

Contents

1	Introduction	1
2	Superconductivity	5
2.1	Ginzburg-Landau Theory of Superconductivity	6
2.2	Bardeen-Cooper-Schrieffer Theory	14
2.3	Dynamical Mean-Field Theory	21
2.4	Quantum Geometry	28
3	Decorated Graphene Model	30
3.1	Lattice Structure	31
3.2	Quantum Geometry	35
4	Application of the Finite-Momentum Method	36
4.1	Decorated Graphene Model	37
4.2	One-Band Hubbard Model on the Square Lattice	45
5	Conclusion	50
A	Other Methods to Extract Superconducting Length Scales	51
B	Computational Implementation and Data Availability	52
	Bibliography	54
	Not cited	63
	Listings	65
	List of Figures	65
	List of Abbreviations	66

Todo list

Description: macroscopic quantum mechanics	1
BCS theory	1
Some more words on characterization: unconventional, high TC, strongly correlated/coupling	1
Experimental measurement of length scales	2
Regimes	2
describe figure	2
difference between condensing and SC	2
BEC regime: TC is given by DS	2
Optimization of TC, need access to SC length scales	2
Introduction to Graphene historically	3
check gap calculation again with assymetric definition of $q!$	19
Write up notes about quantum metric and superfluid weight	29
Write more about the bands	34
Derivative of $h(k)$	34
Section about quantum geometry, maybe with lattice site local quantum metric?	35
This	38
Notable things in plot	41
Plot SC length scales vs V or vs U? between different gaps?	44
Plot MF and DMFT xi and lambda against U	49
Plot DS from Aalto formula vs MF and DMFT DS	49

1

Introduction

The United Nations declared 2025 the ‘International Year of Quantum Science and Technology’ [1]. This is an effort is to raise awareness of the importance of quantum science and its applications, which focuses in 3 key areas: quantum computing, quantum communications and quantum sensors. One effect underlying many of these applications is the phenomenon of superconductivity. For example, superconducting qubits are a promising platform for scalable quantum computing [2, 3] and the Josephson effect [4] can be used to build extremely sensitive measurement devices for magnetic fields [5] or voltages [6].

Superconductivity was discovered in 1911, when Heike Onnes measured that the electrical resistance of Mercury suddenly vanished completely when cooling it below 4 K [7]. In the following decades, more effects in superconducting materials were discovered such as the Meissner effect, the perfect expulsion of external magnetic fields [8]. The theoretical description

Description:
macroscopic
quantum
mechanics

BCS theory

Unconventional Superconductivity

In 1986 and 1987, superconductivity with very high T_C of 30 K (the highest T_C until then was 23.7 K in Nb_3Ge) was discovered in cuprates [9, 10]. Cuprate superconductors are made up of layers of cooper oxide and charge reservoirs in between. The specific charge reservoir layers determine the properties of the superconducting and varying them lead to the discovery of a rich zoo of materials with high T_C [11]. Cuprates are the prime example of the class of superconductors that cannot be explained by BCS theory. They are called unconventional. Mechanisms of pairing are something else than the electron-phonon interaction in BCS-theory, i.e. purely electronic mechanisms. In Cuprates, parent state is a Mott insular (insulator emerging from strong electronic correlations). This means it cannot be explained by BCS theory, because there the parent state is a Fermi liquid.

HTSC not only have higher T_C , so that lower-cost cooling methods can be employed, they also support stronger currents and can withstand higher magnetic fields until SC breaks down. These three parameters span the critical surface

Some more words on characterization: unconventional, high T_C , strongly correlated/coupling

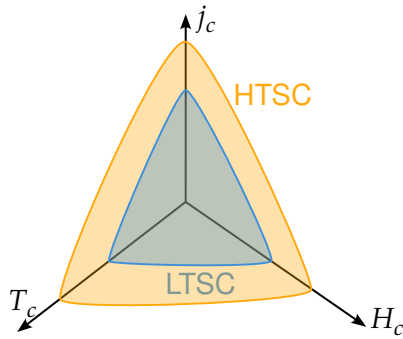


Figure 1.1 – Critical surface of a superconductor. For practical applications, this surface is desired to be as large as possible, making it possible to carry high currents and generate strong magnetic fields while not needing to cool the superconductor to very low temperatures. This generally is the case for high-temperature superconductors in comparison to low-temperature superconductors.

(see fig. 1.1), should be largest for technical applications. So for HTSC, largest commercial application to date is in magnetic resonance imaging, a medical technique using strong magnetic fields and field gradients [12]. There is cable development [13, 14] utilizing the high critical currents.

Critical currents and magnetic fields closely linked to two length scales in SCs: the coherence length ξ_0 and the London penetration depth $\lambda_{L,0}$. Coherence length is linked to size of Cooper pairs, London penetration depth describes how far magnetic fields penetrate into a SC. These length scales are a further characterization of SCs. For example, SC can be split up into type I and type II. The difference is in the response to magnetic fields. In type I SC, sc order is destroyed for fields higher than a critical magnetic field H_C . Type II superconductors have two critical fields H_{C_1}, H_{C_2} , $H_{C_1} > H_{C_2}$. For fields higher than H_{C_1} , the superconducting state is completely destroyed. For fields higher than H_{C_2} but lower than H_{C_1} , the superconducting order is not destroyed, but magnetic field lines penetrate the material. To characterize SC materials, especially SCs with strong correlations it is very desirable to calculate the length scales in ab-initio frameworks.

Experimental measurement of length scales

BCS-BEC Crossover

Topic in the context of high T_C SCs. Framework independent of pairing mechanism. Two regimes can be connected by _____

Regimes

Figure 1.2 shows the _____

describe figure

The intermediate region is characterized by the fact that the [15]

difference between condensing and SC

BEC regime: T_C is given by DS

Optimization of T_C , need access to SC length scales

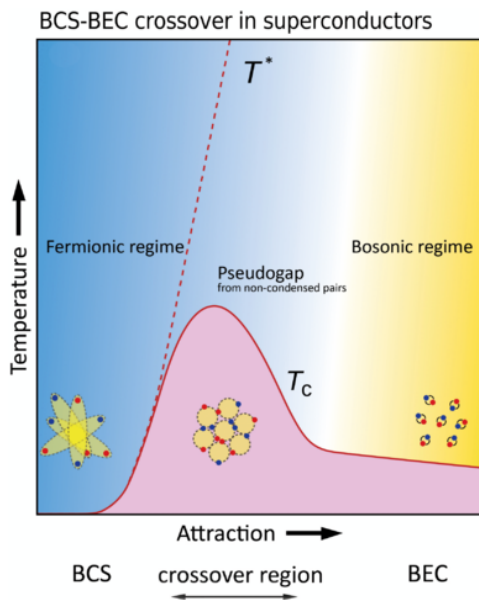


Figure 1.2 – BCS-BEC crossover.
Reprinted figure with permission from [15]. Copyright 2024 by the American Physical Society.

Graphene Structures as a Platform for Correlated Physics

Following the 2018 discovery of superconductivity in twisted bilayer Graphene [16], graphene-based systems gained a renewed interest as a platform for strongly correlated physics. Two methods to engineer strong electron correlations emerged: twisted multilayer systems [16–20] and multilayer systems without twisting, such as Bernal bilayer, ABC or ABCA layered systems [21]. Through different means, electrons in these systems become localized so that interaction effects get more strongly pronounced. Connecting both kind of systems is the strong quantum geometry coming from the Graphene Dirac cones [22], which plays a role in stabilizing superconducting [17, 23] and magnetic order [24, 25].

One interesting development is in twisted multilayer systems, first realized as twisted bilayer Graphene [16]. In comparison to the complex crystal structure of e.g. the Cuprates, twisted multilayer systems have a very simple structure and can be tuned very easily: the angle of twist between the layers can be easily accessed experimentally. The defining feature of these systems are flat electronic bands due to folding of the Brillouin zone. Superconductivity in these systems is enhanced due to the fact that in the flat bands, interactions

Introduction
to Graphene
historically

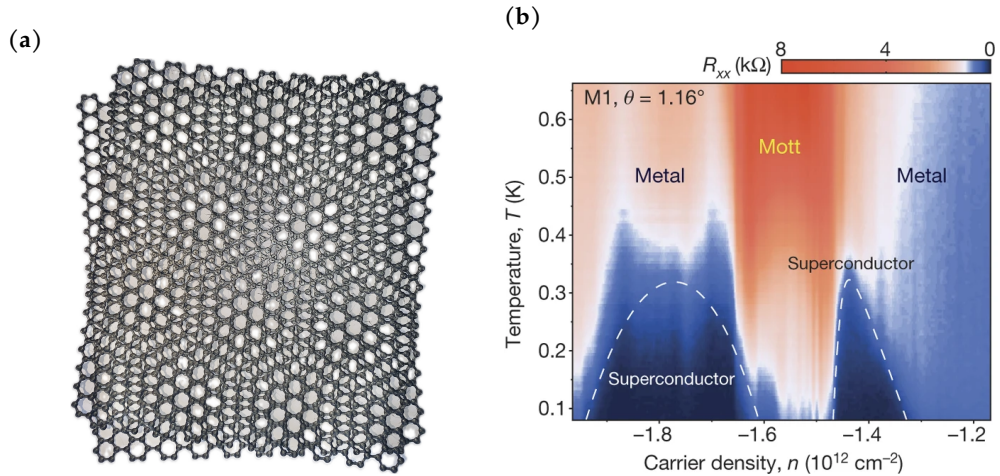


Figure 1.3 – (a) Twisted Bilayer Graphene **(b)** Reproduced from [16] with permission from Springer Nature.

between the electrons are very strongly enhanced. Thus these systems are a very interesting playground to study strongly correlation effects in general and superconductivity in particular.

Organization of this thesis

chapter 2

chapter 3

chapter 4

chapter 5

2

Superconductivity

Superconductivity research has been pushing our understanding of quantum and material science [26]. In this chapter I will review the concepts necessary for understanding superconductivity and introduce the tools used to study it in the later chapters. There are many textbooks covering these topics which can be referenced for a more detailed treatment, such as refs. [27–31].

The superconducting state is a condensation of electrons into pairs with a macroscopically coherent phase, which spontaneously breaks the $U(1)$ phase rotation symmetry. This fixed phase leads to superfluidity in neutral atoms like H_4 or cold atomic gases and superconductivity in superconductors, which can both be phenomenologically explained in Ginzburg-Landau theory, discussed in section 2.1. Both phenomena are characterized by dissipationless flow, of neutral atoms in one case and charged electron pairs in the other. For this reason, similar nomenclature is used, for example the current in a superconductor is often called a charged superflow.

Ginzburg-Landau theory introduces two length scales inherent to superconductors: the coherence length ξ_0 describing the length scale of amplitude variations of the order parameter and the London penetration depth λ_L , which is connected to energy cost of phase variations of the order parameter. They also connect to the energy gap Δ and the condensate stiffness D_S , which are often competing energy scales in superconductors.

The interplay of these length (energy) scales determine the macroscopic properties of a superconductors, so there is a great interest in accessing them from microscopic theories. To this end, section 2.1 also introduces a theoretical framework based on Cooper pairs with finite momentum [32] that will be used in later chapters to calculate these length scales from microscopic theories. Two of these microscopic theories, BCS (Bardeen-Cooper-Schrieffer) theory and DMFT (Dynamical Mean Field Theory) will be introduced in section 2.2 and section 2.3 respectively.

Furthermore, section 2.4 introduces an emerging perspective in the study of novel superconductors: it turns out that the superfluid weight is connected to a property of the electronic band structure called the quantum metric [33, 34].

2.1 Ginzburg-Landau Theory of Superconductivity

Spontaneous Symmetry Breaking and Order Parameter

Symmetries are a powerful concept in physics. Noethers theorem [35] connects the symmetries of physical theories to associated conservation laws. An interesting facet of symmetries in physical theories is the fact that a ground state of a system must not necessarily obey the same symmetries of its Hamiltonian. So for a symmetry operation that is described by a unitary operator U , the Hamiltonian commutes with U , which results in expectation values of the Hamiltonian being invariant under the symmetry operation, but the states $|\phi\rangle$ and $U|\phi\rangle$ can be different. This phenomenon is called spontaneous symmetry breaking and the state $|\phi\rangle$ is said to be symmetry-broken.

One consequence of this fact is that for a given symmetry-broken state $|\phi\rangle$, there exist multiple states with the same energy that can be reached by repeatedly applying U to $|\phi\rangle$. To differentiate the symmetry-broken states an operator can be defined that has all these equivalent states as eigenvectors with different eigenvalues and zero expectation value for symmetric states. This is the microscopic notion of an order parameter.

The original notion of an order parameter was motivated from macroscopic observables that can then be related to the microscopic order parameter operator introduced above. Macroscopically one characterizes the symmetry breaking by an order parameter Ψ which generally can be a complex-valued vector that becomes non-zero below the transition temperature T_C

$$|\Psi| = \begin{cases} 0 & T \geq T_C \\ |\Psi_0| > 0 & T < T_C \end{cases}. \quad (2.1)$$

In the example of a ferromagnet, a finite magnetization of a material is associated with a finite expectation value for the z-component of the spin operator, $m_z = \langle \hat{S}_z \rangle$ [36]. Similarly to a magnetically ordered state, the superconducting state is characterized by an order parameter. The theory of phase transitions in superconductors was developed by Ginzburg and Landau [37]. Landau theory and conversely Ginzburg-Landau theory is not concerned with the the microscopic properties of the order parameter, but describes the changes in thermodynamic properties of matter when the order parameter assumes a finite value. In the context of superconductivity, the order parameter is a complex

quantity

$$\Psi = \Psi_1 + i\Psi_2 = |\Psi|e^{i\phi}. \quad (2.2)$$

and is connected to the pairing amplitude

$$\Delta_{\mathbf{k}} = - \sum_{\mathbf{k}'} V_{\mathbf{k}, \mathbf{k}'} \langle c_{-\mathbf{k}'\downarrow} c_{\mathbf{k}'\uparrow} \rangle, \quad (2.3)$$

i.e. the expectation value for the coherent creation of electron pairs of opposite momentum and spin.

Landau and Ginzburg-Landau Theory

Underlying Landau theory is the concept of the free energy: it is a thermodynamic potential as a function of state variables that is minimized in thermodynamic equilibrium. The fundamental idea of Landau theory is now to write the free energy $F[\Psi]$ as function of the order parameter Ψ and expand it as a polynomial:

$$F_L[\Psi] = \int d^d x f_L[\Psi], \quad (2.4)$$

where

$$f_L[\Psi] = \frac{r}{2}\Psi^2 + \frac{u}{4}\Psi^4 \quad (2.5)$$

is called the free energy density. The stationary point of f_L can be found from the condition

$$\frac{\delta f_L}{\delta \Psi} = r\Psi + u\Psi^3 \stackrel{!}{=} 0 \quad (2.6)$$

which gives

$$\Psi = 0 \vee \Psi = \pm \sqrt{\frac{r}{u}} \quad (2.7)$$

For a stable systems $r > 0$ is required, so for the order parameter to assume a finite value at a critical temperature T_C , the parameter r needs to change sign:

$$r = a(T - T_C). \quad (2.8)$$

Figure 2.1a shows the free energy as a function of a single-component, real order parameter Ψ . When the order parameter can be calculated from a microscopic theory, the critical temperature T_C can be extracted from the behavior of the order parameter near T_C via a linear fit of

$$|\Psi|^2 \propto T_C - T. \quad (2.9)$$

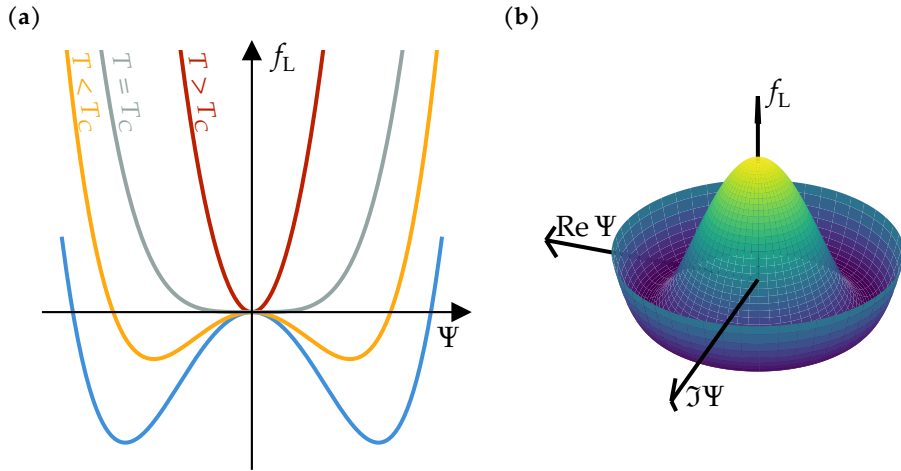


Figure 2.1 – Landau free energy and Mexican hat potential (a) Landau free energy f_L for a real-valued order parameter Ψ at different temperatures T . (b) Landau free energy for a complex order parameter Ψ .

The Landau free energy for a complex order parameter takes the form

$$f_L[\Psi] = r\Psi^*\Psi + \frac{u}{2}(\Psi^*\Psi)^2 = r|\Psi|^2 + \frac{u}{2}|\Psi|^4 \quad (2.10)$$

with again

$$r = a(T_C - T). \quad (2.11)$$

Instead of the two minima, the free energy here has rotation symmetry, since it is independent of the phase of the order parameter:

$$f_L[\Psi] = f_L[e^{i\phi}\Psi]. \quad (2.12)$$

This results in the so called ‘Mexican hat’ potential shown in fig. 2.1b. In this potential, the phase of the order parameter can be rotated continuously, so that there is actually a continuum of symmetry-broken states.

In 1950, V. L. Ginzburg and L.D. Landau published their theory of superconductivity, based on Landau’s theory of phase transitions [37]. Where Landau theory as described above has an uniform order parameter, Ginzburg-Landau theory accounts for it being spatially inhomogeneous, which in turn leads to the order parameter developing a fixed phase. As will be explained in this

section, this fixed phase is the underlying reason for the dissipationless flow in superfluid and superconductors.

The Ginzburg-Landau free energy for a complex order parameter is

$$f_{\text{GL}}[\Psi, \Delta\Psi] = \frac{\hbar^2}{2m^*} |\Delta\Psi|^2 + r|\Psi|^2 + \frac{u}{2}|\Psi|^4, \quad (2.13)$$

where the gradient term $\Delta\Psi$ is added in comparison to the Landau free energy. The prefactor $\frac{\hbar^2}{2m^*}$ is chosen to illustrate the interpretation of the Ginzburg-Landau free energy as the energy of a condensate of bosons, where the gradient term $|\Delta\Psi|^2$ is the kinetic energy.

The free energy in eq. (2.13) is sensitive to a twist of the phase of the order parameter. Writing $\Psi = |\Psi|e^{i\phi}$, the gradient term reads

$$\Delta\Psi = (\Delta|\Psi| + i\Delta\phi|\Psi|)e^{i\phi}. \quad (2.14)$$

With that, eq. (2.13) becomes

$$f_{\text{GL}} = \frac{\hbar^2}{2m^*} |\Psi|^2 (\Delta\phi)^2 + \left[\frac{\hbar^2}{2m^*} (\Delta|\Psi|)^2 + r|\Psi|^2 + \frac{u}{2}|\Psi|^4 \right]. \quad (2.15)$$

Now the contributions of phase and amplitude variations are split up: the first term describes the energy cost of variations in the phase of the order parameter and the second term describes the energy cost of variations in the magnitude of the order parameter.

The dominating fluctuation is determined by the ratio of the factors $\frac{\hbar^2}{2m^*}$ and r , which has the dimension $(\text{Length})^2$, from which one can define the correlation length

$$\xi = \sqrt{\frac{\hbar^2}{2m^*|r|}} = \xi_0 \left(1 - \frac{T}{T_C}\right)^{-\frac{1}{2}} \quad (2.16)$$

with the zero temperature value defined as the coherence length $\xi_0 = \xi(T=0) = \sqrt{\frac{\hbar^2}{2maT_C}}$. On length scales above ξ , the physics is entirely controlled by the phase degrees of freedom, i.e.:

$$f_{\text{GL}} = \frac{\hbar^2}{2m^*} |\Psi|^2 (\Delta\phi)^2 + \text{const.} \quad (2.17)$$

$$= \frac{\hbar^2}{4m^*} n_S (\Delta\phi)^2 + \text{const.} \quad (2.18)$$

$$= D_S (\Delta\phi)^2 + \text{const.} \quad (2.19)$$

where $\frac{n_s}{2} = |\Psi|^2$ is the density of single electrons which form the Cooper pairs, also called the superfluid or superconducting density. Equation (2.19) shows that twisting the phase of the condensate is associated with an energy cost. This energy cost is characterized by the superfluid phase stiffness D_S .

Assuming frozen amplitude fluctuations $\Delta|\Psi(\mathbf{r})| = 0$, the stationary point of eq. (2.15) is

$$|\Psi| = |\Psi_0| \sqrt{1 - \xi^2 |\Delta\phi(\mathbf{r})|^2}. \quad (2.20)$$

This shows that the superconducting order gets suppressed and eventually destroyed by short-ranged (below ξ) phase fluctuations. By introducing a particular form of phase fluctuations $\phi = \mathbf{q} \cdot \mathbf{r}$ into a microscopic model, it is possible to probe this breakdown of superconductivity and thus gain insight into the nature of superconductivity, in particular this gives access to ξ . This method will be explained further in a later section.

The discussion so far is valid for neutral superfluids, but superconductors are charged superfluids, so they couple to electromagnetic fields. The Ginzburg-Landau free energy with minimal coupling to an electromagnetic field is

$$f_{\text{GL}}[\Psi, \mathbf{A}] = \frac{\hbar^2}{2m^*} \left| \left(\Delta - \frac{ie^*}{\hbar} \mathbf{A} \right) \Psi \right|^2 + r|\Psi|^2 + \frac{u}{2}|\Psi|^4 + \frac{B^2}{2\mu_0}. \quad (2.21)$$

with an additional term to include the electromagnetic energy of the magnetic field $\mathbf{B} = \nabla \times \mathbf{A}$. It describes two intertwined Ginzburg-Landau theories for Ψ and \mathbf{A} . This means there are two length scales, the coherence length ξ governing amplitude fluctuations of Ψ and the London penetration depth λ_L which is associated with variations of the vector potential \mathbf{A} . This can be seen by considering a homogeneous condensate $\Psi = \sqrt{n_s/2}$, such that the free energy only depends on the vector potential as

$$f_{\text{GL}}[\mathbf{A}] \sim \frac{e^2 n_s}{2m^*} A^2 + \frac{(\nabla \times \mathbf{A})^2}{2\mu_0} = \frac{1}{2\mu_0} \left(\frac{1}{\lambda_L^2} A^2 + (\nabla \times \mathbf{A})^2 \right) \quad (2.22)$$

with the London penetration depth

$$\lambda_L = \sqrt{\frac{m^*}{e^2 n_s \mu_0}} \quad (2.23)$$

as the prefactor of A^2 , i.e. it is associated with the variations of \mathbf{A} . It is connected to the condensate stiffness as

$$\lambda_L = \sqrt{\frac{m^*}{e^2 n_s \mu_0}} = \sqrt{\frac{\hbar^2}{4e^2 \mu_0} \frac{4m^*}{\hbar^2 n_s}} = \sqrt{\frac{\hbar^2}{4e^2 \mu_0} \frac{1}{D_s}}, \quad (2.24)$$

see eq. (2.19).

The current density can be calculated from the stationary point condition of the free energy w.r.t. the vector potential \mathbf{A}

$$\frac{\delta f_{\text{GL}}}{\delta \mathbf{A}} = -\mathbf{j} + \frac{1}{\mu_0} \nabla \times \mathbf{B} \stackrel{!}{=} 0 \quad (2.25)$$

defining the supercurrent density

$$\mathbf{j} = -i \frac{e\hbar}{m^*} (\Psi^* \Delta \Psi - \Psi \Delta \Psi^*) - \frac{4e^2}{m^*} |\Psi|^2 \mathbf{A}. \quad (2.26)$$

Introducing the order parameter with a fixed phase $\Psi = |\Psi| e^{i\phi}$ gives

$$\mathbf{j} = 2e|\Psi|^2 \frac{\hbar}{m^*} \left(\nabla \phi - \frac{2\pi}{\Phi_0} \mathbf{A} \right) \quad (2.27)$$

with the magnetic flux quantum $\Phi_0 = \frac{\pi\hbar}{e}$. This shows that not only an applied field \mathbf{A} can induce a supercurrent, but also the phase twist $\nabla\phi$ of the condensate ground state, which is the remarkable property of superconductors enabling the dissipationless current. Where a conventional current is achieved by excitations above the ground state, the superflow is achieved through deformation of the ground-state phase. The supercurrent can be gauge-transformed to

$$\mathbf{j} = -\frac{4e^2 n_s}{m^*} \mathbf{A} = \tilde{D}_S \mathbf{A} \quad (2.28)$$

which shows that the superfluid phase stiffness

$$D_S = \frac{\hbar^2}{(2e)^2} \tilde{D}_S \quad (2.29)$$

also encodes the linear response of a system to a small applied vector field \mathbf{A} .

Calculating Superconducting Length Scales

As previously discussed in the context of eq. (2.20), analyzing the breakdown of the order parameter with phase fluctuations provides insight into the coherence length ξ_0 and the London penetration depth λ_L . A particular choice of phase fluctuations would be

$$\phi(\mathbf{r}) = \mathbf{q} \cdot \mathbf{r}, \quad (2.30)$$

which corresponds to Cooper pairs with a finite center-of-mass momentum \mathbf{q} . Although Cooper pairs typically do not carry such momentum in most materials, superconducting states with finite momentum can emerge under the influence of external fields or magnetism [38–40].

This approach for examining superconducting length scales that is also the was developed by Witt et al. [32]. The authors used the method to characterize superconductivity in alkali-doped fullerides, a material noted for its strong electronic correlations. They find that via multiorbital effects, a superconducting state characterized by a short coherence length yet robust stiffness, alongside a domeless increase in critical temperature with increasing pairing interaction. This is in contrast to the usual BCS-BEC crossover phenomenology that can be seen in unconventional superconductors, where with increasing pairing interaction there is a maximum of the critical temperature. This shows that understanding superconducting length scales is particularly crucial in the characterization of new high T_C superconductors.

This section introduces the method within the framework of Ginzburg-Landau theory. The integration of this method into microscopic theories such as BCS theory and DMFT will be covered in the respective subsequent sections.

The phase fluctuation in eq. (2.30) corresponds to Fulde–Ferrell (FF) type pairing [41]

$$\Psi_{\mathbf{q}}(\mathbf{r}) = |\Psi_{\mathbf{q}}| e^{i\mathbf{q}\mathbf{r}}. \quad (2.31)$$

With that, the free energy density eq. (2.13) is

$$f_{GL}[\Psi_{\mathbf{q}}] = r|\Psi_{\mathbf{q}}|^2 + \frac{u}{2}|\Psi_{\mathbf{q}}|^4 + \frac{\hbar^2 q^2}{2m^*}|\Psi_{\mathbf{q}}|^2. \quad (2.32)$$

The stationary point of the system can again be found via the condition

$$\frac{\delta f_{GL}}{\delta \Psi_{\mathbf{q}}^*} = 2\Psi_{\mathbf{q}} \left[r(1 - \xi^2 q^2) + u|\Psi_{\mathbf{q}}|^2 \right] = 0, \quad (2.33)$$

which results in the \mathbf{q} -dependence of the order parameter

$$|\Psi_{\mathbf{q}}|^2 = |\Psi_0|^2 (1 - \xi(T)^2 q^2) . \quad (2.34)$$

This can be seen in fig. 2.2a. So for some value \mathbf{q}_c , the kinetic energy from phase modulations exceeds the gain in energy from pairing and superconducting order breaks down

$$\psi_{\mathbf{q}_c} = 0 . \quad (2.35)$$

So in Ginzburg-Landau theory the correlation length can be calculated via

$$q_c = \xi(T)^{-1} . \quad (2.36)$$

The temperature dependence of the $\xi(T)$ then gives access to the coherence length via eq. (2.16)

$$\xi(T) = \xi_0 \left(1 - \frac{T}{T_C} \right)^{-\frac{1}{2}} \quad (2.37)$$

Equation (2.26) shows that the momentum of the Cooper pairs entails a supercurrent $\mathbf{j}_{\mathbf{q}}$. With $\phi(\mathbf{r}) = \mathbf{q} \cdot \mathbf{r}$ and $\mathbf{A} = 0$, the current is

$$\mathbf{j}_{\mathbf{q}} = \frac{2he}{m^*} |\Psi_{\mathbf{q}}|^2 \mathbf{q} . \quad (2.38)$$

The current $\mathbf{j}_{\mathbf{q}}$ is a non-monotonous function of \mathbf{q} with a maximum called the depairing current j_{dp} as can be seen in fig. 2.2b. The depairing current is an upper boundary for the maximal current that can flow through a material, also called the critical current j_c . The value of j_c is strongly dependent on the geometry of the sample [42, 43], so j_{dp} is not necessarily experimentally available, but it can be used to calculate the London penetration depth [28]

$$\lambda_L(T) = \sqrt{\frac{\Phi_0}{3\sqrt{3}\pi\mu_0\xi(T)j_{dp}(T)}} = \lambda_{L,0} \left(1 - \left(\frac{T}{T_C} \right)^4 \right)^{-\frac{1}{2}} \quad (2.39)$$

The superfluid phase stiffness can then be calculated via eq. (2.24)

$$D_S \propto \lambda_L^{-2} . \quad (2.40)$$

The finite-momentum method in the limit of $\mathbf{q} \rightarrow 0$ is related to linear response techniques to calculate the superfluid weight [23, 33].

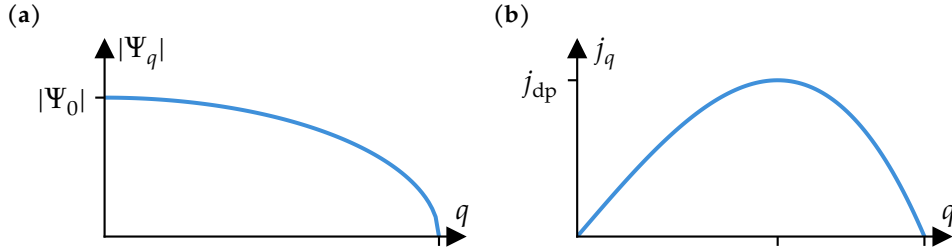


Figure 2.2 – Ginzburg-Landau solutions for a finite momentum q . (a) Breakdown of the order parameter with q , the critical q_c is the point at which the order parameter is 0. (b) Superconducting current coming from the finite momentum of the Cooper pairs. The maximum of the current with q is called the depairing current j_{dp} .

2.2 Bardeen-Cooper-Schrieffer Theory

The BCS (Bardeen-Cooper-Schrieffer) description of superconductivity was the first microscopic theory, identifying condensation of electrons into pairs forming a macroscopic quantum state as the underlying mechanism [44]. The BCS-Hamiltonian is

$$H_{BCS} = \sum_{\mathbf{k}\sigma} \epsilon_{\mathbf{k}\sigma} c_{\mathbf{k}\sigma}^\dagger c_{\mathbf{k}\sigma} + \sum_{\mathbf{k},\mathbf{k}'} V_{\mathbf{k},\mathbf{k}'} c_{\mathbf{k}\uparrow}^\dagger c_{-\mathbf{k}\downarrow}^\dagger c_{-\mathbf{k}'\downarrow} c_{\mathbf{k}'\uparrow}, \quad (2.41)$$

where $V_{\mathbf{k},\mathbf{k}'}$ is a model interaction. It describes a phonon-mediated attractive interaction for energies lower than the Debye frequency ω_D :

$$V_{\mathbf{k},\mathbf{k}'} = \begin{cases} -V_0 & (\epsilon_{\mathbf{k}}, \epsilon_{\mathbf{k}'} < \omega_D) \\ 0 & (\text{otherwise}) \end{cases}. \quad (2.42)$$

The BCS Hamiltonian can be treated in a mean-field approach, writing

$$\begin{aligned} \sum_{\mathbf{k},\mathbf{k}'} V_{\mathbf{k},\mathbf{k}'} c_{\mathbf{k}\uparrow}^\dagger c_{-\mathbf{k}\downarrow}^\dagger c_{-\mathbf{k}'\downarrow} c_{\mathbf{k}'\uparrow} &\approx \sum_{\mathbf{k},\mathbf{k}'} V_{\mathbf{k},\mathbf{k}'} \langle c_{\mathbf{k}\uparrow}^\dagger c_{-\mathbf{k}\downarrow}^\dagger \rangle c_{-\mathbf{k}'\downarrow} c_{\mathbf{k}'\uparrow} + V_{\mathbf{k},\mathbf{k}'} c_{\mathbf{k}\uparrow}^\dagger c_{-\mathbf{k}\downarrow}^\dagger \langle c_{-\mathbf{k}'\downarrow} c_{\mathbf{k}'\uparrow} \rangle \\ &= \sum_{\mathbf{k}} \Delta_{\mathbf{k}}^* c_{-\mathbf{k}\downarrow} c_{\mathbf{k}\uparrow} + \Delta_{\mathbf{k}} c_{\mathbf{k}\uparrow}^\dagger c_{-\mathbf{k}\downarrow}^\dagger \end{aligned} \quad (2.43)$$

with the pairing amplitude

$$\Delta_{\mathbf{k}} = - \sum_{\mathbf{k}'} V_{\mathbf{k},\mathbf{k}'} \langle c_{-\mathbf{k}'\downarrow} c_{\mathbf{k}'\uparrow} \rangle, \quad (2.44)$$

which is also the order parameter in BCS theory. A finite Δ corresponds to the pairing introduced above: it means there is a finite expectation value for a coherent creation/annihilation of electron pairs with opposite momentum and spin.

BCS theory was very successful in two ways: on the one hand it could quantitatively explain effects in the superconductors known at the time, for example the Hebel-Slichter peak that was measured in 1957 [45, 46] and the band gap measured by Giaever in 1960 [47]. On the other hand it gave a microscopic explanation for the phenomenological theories of superconductivity based on F. Londons 1937 description of a quantum-mechanical wave function with a defined phase [48]. This picture of electron pairing still holds today even for superconductors that cannot be described by BCS theory [49].

There exist many textbooks tackling BCS theory from different angles, such as refs. [27, 28]. This section will use the ideas from BCS theory to treat superconductivity in the attractive Hubbard model on a mean-field level.

Multiband BCS Theory

The Hubbard model is regarded as the simplest model for interacting electron systems. It goes back to works by Hubbard [50], Kanamori [51] and Gutzweiler [52] in the 1960s. The Hamiltonian of the single-band Hubbard model is

$$H = H_0 + H_{\text{int}} = \sum_{\langle ij \rangle \sigma} (-t_{i,j} - \mu_\sigma \delta_{i,j}) c_{i,\sigma}^\dagger c_{j,\sigma} + \text{h.c.} + U \sum_i c_{i,\uparrow}^\dagger c_{i,\downarrow}^\dagger c_{i,\downarrow} c_{i,\uparrow} \quad (2.45)$$

where $U > 0$. The interaction describes a repulsive interaction between electrons of different spin at the same lattice site.

The Hubbard interaction is localized to one lattice site, so the Hubbard model emphasizes the electronic correlations due to local interactions. With the discovery of high T_C superconductors in the Cuprates, it was quickly realized that the 2D Hubbard model in the intermediate to strong-coupling regime could describe the CuO₂ layers [53] well. Just as Cuprate materials, the Hubbard model has parameter regimes with $d_{x^2-y^2}$ superconductivity, strong antiferromagnetic correlations, stripe order, pseudogaps, Fermi liquid and bad metallic behavior, with the phase diagram lines and observables being similar as a function of doping and temperature. Besides the relevancy for the Cuprates, having few parameters and simultaneously a very rich phase diagram with a variety of many-body effects also made the Hubbard model a perfect playground for new

numerical tools, among them diagonalization, diagrammatics, tensor network, Quantum Monte Carlo (QMC) methods and DMFT (see section 2.3) [54].

The Hubbard model in the form of eq. (2.45) can be extended in a multitude of ways to model a variety of physical system, in this thesis to multiple orbitals (i.e. atoms in the unit cell for lattice systems) and an attractive interaction. The local attractive interaction in this extended Hubbard model is useful as a model with a simple set of parameters to study superconductivity in systems where electrons experience a strong local attractive interaction mediated through phonon degrees of freedom or with electronic excitations [55]. The form of the Hubbard Hamiltonian is then

$$H = \sum_{\langle i\alpha j\beta \rangle \sigma} (-t_{i\alpha, j\beta} - \mu_\sigma \delta_{i\alpha, j\beta}) c_{i\alpha, \sigma}^\dagger c_{j\beta, \sigma} + \text{h.c.} - \sum_{i, \alpha} U_\alpha c_{i, \alpha, \uparrow}^\dagger c_{i, \alpha, \downarrow}^\dagger c_{i, \alpha, \downarrow} c_{i, \alpha, \uparrow}, \quad (2.46)$$

where α counts orbitals and the minus sign in front of the interaction term is taken as a convention so that $U > 0$ now corresponds to an attractive interaction.

The idea of the mean-field approximation relies on the assumption that operators A do not deviate much from their average value $\langle A \rangle$, meaning the deviation $\delta A = A - \langle A \rangle$ are small. Looking at the interaction term eq. (2.46) and taking the idea of pairing from the BCS Hamiltonian, the deviation operators for pair creation/annihilation operators are

$$\begin{aligned} d_{i, \alpha} &= c_{i, \alpha, \uparrow}^\dagger c_{i, \alpha, \downarrow}^\dagger - \langle c_{i, \alpha, \uparrow}^\dagger c_{i, \alpha, \downarrow}^\dagger \rangle \\ e_{i, \alpha} &= c_{i, \alpha, \downarrow} c_{i, \alpha, \uparrow} - \langle c_{i, \alpha, \downarrow} c_{i, \alpha, \uparrow} \rangle. \end{aligned} \quad (2.47)$$

Using these, the interaction part of the Hamiltonian becomes

$$H_{\text{int}} = - \sum_{i, \alpha} U_\alpha c_{i, \alpha, \uparrow}^\dagger c_{i, \alpha, \downarrow}^\dagger c_{i, \alpha, \downarrow} c_{i, \alpha, \uparrow} \quad (2.48)$$

$$= - \sum_{i, \alpha} U_\alpha (d_{i, \alpha}^\dagger + \langle c_{i, \alpha, \uparrow}^\dagger c_{i, \alpha, \downarrow}^\dagger \rangle) (e_{i, \alpha} + \langle c_{i, \alpha, \downarrow} c_{i, \alpha, \uparrow} \rangle) \quad (2.49)$$

$$\begin{aligned} &= - \sum_{i, \alpha} U_\alpha (d_{i, \alpha} e_{i, \alpha} + d_{i, \alpha} \langle c_{i, \alpha, \downarrow} c_{i, \alpha, \uparrow} \rangle \\ &\quad + e_{i, \alpha} \langle c_{i, \alpha, \uparrow}^\dagger c_{i, \alpha, \downarrow}^\dagger \rangle + \langle c_{i, \alpha, \uparrow}^\dagger c_{i, \alpha, \downarrow}^\dagger \rangle \langle c_{i, \alpha, \downarrow} c_{i, \alpha, \uparrow} \rangle), \end{aligned} \quad (2.50)$$

where the first term is quadratic in the deviations and can be neglected. Thus one arrives at the approximation

$$H_{\text{int}} \approx - \sum_{i,\alpha} U_\alpha (d_{i,\alpha} \langle c_{i,\alpha,\downarrow} c_{i,\alpha,\uparrow} \rangle + e_{i,\alpha} \langle c_{i,\alpha,\uparrow}^\dagger c_{i,\alpha,\downarrow}^\dagger \rangle + \langle c_{i,\alpha,\uparrow}^\dagger c_{i,\alpha,\downarrow}^\dagger \rangle \langle c_{i,\alpha,\downarrow} c_{i,\alpha,\uparrow} \rangle) \quad (2.51)$$

$$= - \sum_{i,\alpha} U_\alpha (c_{i,\alpha,\uparrow}^\dagger c_{i,\alpha,\downarrow}^\dagger \langle c_{i,\alpha,\downarrow} c_{i,\alpha,\uparrow} \rangle + c_{i,\alpha,\downarrow} c_{i,\alpha,\uparrow} \langle c_{i,\alpha,\uparrow}^\dagger c_{i,\alpha,\downarrow}^\dagger \rangle - \langle c_{i,\alpha,\uparrow}^\dagger c_{i,\alpha,\downarrow}^\dagger \rangle \langle c_{i,\alpha,\downarrow} c_{i,\alpha,\uparrow} \rangle) \quad (2.52)$$

$$= \sum_{i,\alpha} \left(\Delta_{i,\alpha} c_{i,\alpha,\uparrow}^\dagger c_{i,\alpha,\downarrow}^\dagger + \Delta_{i,\alpha}^* c_{i,\alpha,\downarrow} c_{i,\alpha,\uparrow} - \frac{|\Delta_{i,\alpha}|^2}{U_\alpha} \right) \quad (2.53)$$

with the local superconducting order parameter

$$\Delta_{i,\alpha} = -U_\alpha \langle c_{i,\alpha,\downarrow} c_{i,\alpha,\uparrow} \rangle . \quad (2.54)$$

This results in the mean-field Hamiltonian

$$H_{\text{MF}} = \sum_{\langle i\alpha j\beta \rangle \sigma} (-t_{i\alpha,j\beta} - \mu_\sigma \delta_{i\alpha,j\beta}) c_{i\alpha,\sigma}^\dagger c_{j\beta,\sigma} + \text{h.c.} + \sum_{i,\alpha} \left(\Delta_{i,\alpha} c_{i,\alpha,\uparrow}^\dagger c_{i,\alpha,\downarrow}^\dagger + \Delta_{i,\alpha}^* c_{i,\alpha,\downarrow} c_{i,\alpha,\uparrow} - \frac{|\Delta_{i,\alpha}|^2}{U_\alpha} \right) \quad (2.55)$$

To include finite momentum in BCS theory, take the ansatz of a Fulde-Ferrel (FF) type pairing [41]:

$$\Delta_{i,\alpha} = \Delta_\alpha e^{i\mathbf{q}\mathbf{r}_{i\alpha}} \quad (2.56)$$

The mean-field Hamiltonian can be written in momentum space using the Fourier transform

$$c_{i\alpha\sigma} = \frac{1}{\sqrt{N}} \sum_{\mathbf{k}} e^{i\mathbf{k}\mathbf{r}_{i\alpha}} c_{\mathbf{k}\alpha\sigma}, \quad (2.57)$$

with position vectors $\mathbf{r}_{i\alpha} = \mathbf{R}_i + \delta_\alpha$, written using the position of the unit cell \mathbf{R}_i and the orbital position inside the unit cell δ_α . Using this, the mean-field Hamiltonian is

$$H_{\text{MF}}(\mathbf{q}) = \sum_{\mathbf{k}} \Psi_{\mathbf{q},\mathbf{k}}^\dagger H_{\text{BdG}}(\mathbf{q}, \mathbf{k}) \Psi_{\mathbf{q},\mathbf{k}} + K_{\mathbf{q}} \quad (2.58)$$

with the Nambu spinors

$$\Psi_{\mathbf{q},\mathbf{k}} = \begin{pmatrix} c_{\mathbf{k}1\uparrow} & c_{\mathbf{k}2\uparrow} & \dots & c_{\mathbf{k}n_{\text{orb}}\uparrow} & c_{\mathbf{q}-\mathbf{k}1\downarrow}^{\dagger} & c_{\mathbf{q}-\mathbf{k}2\downarrow}^{\dagger} & \dots & c_{\mathbf{q}-\mathbf{k}n_{\text{orb}}\downarrow}^{\dagger} \end{pmatrix}^T \quad (2.59)$$

and

$$K_{\mathbf{q}} = \sum_{\mathbf{k}} \text{Tr}[H_{\mathbf{k}}^{\downarrow}] - n_{\text{orb}} N \mu - N \sum_{\alpha} \frac{|\Delta_{\alpha}(\mathbf{q})|^2}{U}. \quad (2.60)$$

The matrix between the spinors is the so-called Bogoliubov-de Gennes (BdG) matrix

$$H_{\text{BdG}}(\mathbf{q}, \mathbf{k}) = \begin{pmatrix} H_{\mathbf{k}}^{\uparrow} - \mu & \Delta(\mathbf{q}) \\ \Delta^{\dagger}(\mathbf{q}) & -\left(H_{\mathbf{q}-\mathbf{k}}^{\downarrow}\right)^* + \mu \end{pmatrix} \quad (2.61)$$

with $H_{0,\sigma}$ being the F.T. of the kinetic term

$$[H_{\mathbf{k}}^{\sigma}] = \sum_i t_{i\alpha,0\beta}^{\sigma} e^{-i\mathbf{k}\cdot(\mathbf{R}_i + \delta_{\alpha} - \delta_{\beta})} \quad (2.62)$$

and the matrix of order parameters, with the \mathbf{q} -dependence made explicit:

$$\Delta = \text{diag}(\Delta_1(\mathbf{q}), \Delta_2(\mathbf{q}), \dots, \Delta_{n_{\text{orb}}}(\mathbf{q})). \quad (2.63)$$

For time-reversal symmetric systems, there exists a solution such that all Δ_{α} are real [33] but the introduction of a finite \mathbf{q} breaks time-reversal symmetry. This means that in a multiband system, the order parameters in the orbital can develop different phases.

In the BdG formulation, the problem is now reduced to diagonalization of the matrix in eq. (2.61), so one can write

$$H_{\text{BdG}} = U_{\mathbf{q},\mathbf{k}} \epsilon_{\mathbf{q},\mathbf{k}} U_{\mathbf{q},\mathbf{k}}^{\dagger} \quad (2.64)$$

with the diagonal matrix $\epsilon_{\mathbf{q},\mathbf{k}} = \text{diag}(\epsilon_1(\mathbf{q}, \mathbf{k}), \epsilon_2(\mathbf{q}, \mathbf{k}), \dots, \epsilon_{2 \cdot n_{\text{orb}}}(\mathbf{q}, \mathbf{k}))$.

The BdG formulation defines a linear transformation from the creation and annihilation to a new set of operators

$$\gamma_{\mathbf{q},\mathbf{k}} = \begin{pmatrix} \gamma_{\mathbf{q},\mathbf{k},1} & \gamma_{\mathbf{q},\mathbf{k},2} & \dots & \gamma_{\mathbf{q},\mathbf{k},2 \cdot n_{\text{orb}}} \end{pmatrix}^T \quad (2.65)$$

via

$$\gamma_{\mathbf{q},\mathbf{k}} = U_{\mathbf{q},\mathbf{k}}^{\dagger} \Psi_{\mathbf{q},\mathbf{k}} \quad (2.66)$$

which define non-interacting quasi-particles. Using these operators, the mean-field Hamiltonian becomes

$$H_{\text{MF}}(\mathbf{q}) = \sum_{\mathbf{k}} \gamma_{\mathbf{q},\mathbf{k}} \epsilon_{\mathbf{q},\mathbf{k}} \gamma_{\mathbf{q},\mathbf{k}}^\dagger \quad (2.67)$$

Mean-field theory does not give a value for the order parameter *a priori*, it needs to be calculated self-consistently using the gap equation

$$\begin{aligned} \Delta_\alpha &= -U_\alpha \langle c_{i,\alpha,\downarrow} c_{i,\alpha,\uparrow} \rangle = -\frac{U}{N} \sum_{\mathbf{k}} \langle c_{\mathbf{q}+\mathbf{k}\alpha,\downarrow} c_{\mathbf{q}-\mathbf{k}\alpha,\uparrow} \rangle \\ &= -\frac{U}{N} \sum_{\mathbf{k}} \sum_{ij} [U_{\mathbf{q}^\dagger, \mathbf{k}}]_{i,\alpha+n_{\text{orb}}} [U_{\mathbf{q}, \mathbf{k}}]_{\alpha,j} \langle \gamma_i^\dagger \gamma_i \rangle \\ &= -\frac{U}{N} \sum_{\mathbf{k}} [U_{\mathbf{q}, \mathbf{k}} n_F(\epsilon_{\mathbf{q}, \mathbf{k}}) U_{\mathbf{q}, \mathbf{k}}^\dagger]_{\alpha,\alpha+n_{\text{orb}}} . \end{aligned} \quad (2.68)$$

check gap calculation again with assymetric definition of q!

This means starting from an initial value, the BdG matrix needs to be set up, diagonalized and then used to determine Δ_α again, until a converged value is found.

To implement the finite \mathbf{q} method to calculate the superconducting length scales, one also needs access to the supercurrent in BCS theory. In general, a current \mathbf{j} is induced by change of the local polarization \mathbf{P} . The polarization operator given by

$$\hat{\mathbf{P}} = e \sum_{i\alpha} \mathbf{R}_{i\alpha} c_{i\alpha}^\dagger c_{i\alpha} = e \sum_{i\alpha} \mathbf{R}_{i\alpha} n_{i\alpha} , \quad (2.69)$$

so that the current given by the time derivative of the polarization operator is

$$\hat{\mathbf{j}} = \dot{\hat{\mathbf{P}}} = \frac{i}{\hbar} [\hat{\mathbf{P}}, H] . \quad (2.70)$$

Taking a Hamiltonian with pairing $\Delta_{i,\alpha}$

$$H = \sum_{(i\alpha j\beta)\sigma} -t_{i\alpha,j\beta} c_{i\alpha,\sigma}^\dagger c_{j\beta,\sigma} + \sum_{i,\alpha} (\Delta_{i,\alpha} c_{i,\alpha,\uparrow}^\dagger c_{i,\alpha,\downarrow}^\dagger + \Delta_{i,\alpha}^* c_{i,\alpha,\downarrow} c_{i,\alpha,\uparrow}) =: H_N + H_{\text{AN}} \quad (2.71)$$

one needs to calculate three kinds of commutators for eq. (2.70):

$$[n_{m\gamma}, c_{i\alpha}^\dagger c_{j\beta}] = c_{i\alpha}^\dagger [n_{m\gamma}, c_{j\beta}] + [n_{m\gamma}, c_{i\alpha}^\dagger] c_{j\beta} = (\delta_{m\gamma,i\alpha} - \delta_{m\gamma,j\beta}) c_{i\alpha}^\dagger c_{j\beta} \quad (2.72)$$

$$[n_{m\gamma}, c_{i\alpha} c_{i\alpha}] = c_{i\alpha} [n_{m\gamma}, c_{i\alpha}] + [n_{m\gamma}, c_{i\alpha}] c_{i\alpha} = -2\delta_{m\gamma,i\alpha} c_{i\alpha} c_{i\alpha} \quad (2.73)$$

$$[n_{m\gamma}, c_{i\alpha}^\dagger c_{i\alpha}^\dagger] = c_{i\alpha}^\dagger [n_{m\gamma}, c_{i\alpha}^\dagger] + [n_{m\gamma}, c_{i\alpha}^\dagger] c_{i\alpha}^\dagger = 2\delta_{m\gamma,i\alpha} c_{i\alpha}^\dagger c_{i\alpha}^\dagger . \quad (2.74)$$

Using these, the normal and anomalous component of the current can be calculated:

$$\begin{aligned}\hat{\mathbf{j}}_N &= \frac{i}{\hbar} [\hat{\mathbf{P}}, H_N] = -i\frac{e}{\hbar} \sum_{i\alpha, j\beta, m\gamma} \mathbf{R}_{m\gamma} t_{i\alpha, j\beta} [n_{m\gamma}, c_{i\alpha}^\dagger c_{j\beta}] \\ &= -i\frac{e}{\hbar} \sum_{i\alpha, j\beta, m\gamma} \mathbf{R}_{m\gamma} t_{i\alpha, j\beta} (\delta_{m\gamma, i\alpha} - \delta_{m\gamma, j\beta}) c_{i\alpha}^\dagger c_{j\beta} \\ &= -i\frac{e}{\hbar} \sum_{i\alpha, j\beta} (\mathbf{R}_{i\alpha} - \mathbf{R}_{j\beta}) t_{i\alpha, j\beta} c_{i\alpha}^\dagger c_{j\beta}\end{aligned}\quad (2.75)$$

$$\begin{aligned}\hat{\mathbf{j}}_{AN} &= \frac{i}{\hbar} [\hat{\mathbf{P}}, H_{AN}] = -i\frac{e}{\hbar} \sum_{i\alpha, m\gamma} \mathbf{R}_{m\gamma} (\Delta_{i\alpha} [n_{m\gamma}, c_{i\alpha} c_{i\alpha}] + \Delta_{i\alpha}^* [n_{m\gamma}, c_{i\alpha}^\dagger c_{i\alpha}^\dagger]) \\ &= -i\frac{2e}{\hbar} \sum_{i\alpha, m\gamma} \mathbf{R}_{m\gamma} (-\delta_{m\gamma, i\alpha} \Delta_{i\alpha} c_{i\alpha} c_{i\alpha} + \delta_{m\gamma, i\alpha} \Delta_{i\alpha}^* c_{i\alpha}^\dagger c_{i\alpha}^\dagger) \\ &= i\frac{2e}{\hbar} \sum_{i\alpha} \mathbf{R}_{i\alpha} (-\Delta_{i\alpha} c_{i\alpha} c_{i\alpha} + \Delta_{i\alpha}^* c_{i\alpha}^\dagger c_{i\alpha}^\dagger).\end{aligned}\quad (2.76)$$

The expectation value of the anomalous part vanishes

$$\langle \hat{\mathbf{j}}_{AN} \rangle = i\frac{2e}{\hbar} \sum_{i\alpha} \mathbf{R}_{i\alpha} (-\Delta_{i\alpha} \langle c_{i\alpha} c_{i\alpha} \rangle + \Delta_{i\alpha}^* \langle c_{i\alpha}^\dagger c_{i\alpha}^\dagger \rangle) \quad (2.77)$$

$$= i\frac{2e}{\hbar} \sum_{i\alpha} \mathbf{R}_{i\alpha} (-\Delta_{i\alpha} \Delta_{i\alpha}^* + \Delta_{i\alpha}^* \Delta_{i\alpha}) = 0, \quad (2.78)$$

so that the current density is given by the normal component.

Using the Fourier transform

$$c_{i\alpha\sigma} = \frac{1}{\sqrt{N}} \sum_{\mathbf{k}} e^{i\mathbf{k}\mathbf{r}_{i\alpha}} c_{\mathbf{k}\alpha\sigma}, \quad (2.79)$$

the current can be written as

$$\hat{\mathbf{j}} = \hat{\mathbf{j}}_N = i \frac{e}{\hbar} \frac{1}{N_k} \sum_{i\alpha, j\beta, v b k k'} (\mathbf{R}_{i\alpha} - \mathbf{R}_{j\beta}) t_{i\alpha, j\beta} e^{i(\mathbf{k}r_{i\alpha} - \mathbf{k}'r_{j\beta})} c_{\mathbf{k}\alpha}^\dagger c_{\mathbf{k}'\beta} \quad (2.80)$$

$$= i \frac{e}{\hbar} \frac{1}{N_k} \sum_{i\alpha, j\beta, \mathbf{k}\mathbf{k}'} (\mathbf{R}_{i\alpha} - \mathbf{R}_{j\beta}) t_{i\alpha, j\beta} e^{i(\mathbf{k}r_{i\alpha} - \mathbf{k}'r_{j\beta})} c_{\mathbf{k}\alpha}^\dagger c_{\mathbf{k}'\beta} \quad (2.81)$$

$$\stackrel{\mathbf{r}_{i\alpha} \rightarrow \mathbf{r}_{i\alpha} + \mathbf{r}_{j\beta}}{=} i \frac{e}{\hbar} \frac{1}{N_k} \sum_{\mathbf{r}_{i\alpha} \mathbf{k}\mathbf{k}' \alpha \beta \sigma} \mathbf{R}_{i\alpha} t_{i\alpha, j\beta} \sum_{\mathbf{r}_{j\beta}} e^{i(\mathbf{k} - \mathbf{k}') \mathbf{r}_{j\beta}} c_{\mathbf{k}\alpha}^\dagger c_{\mathbf{k}'\beta} \quad (2.82)$$

$$= \frac{e}{\hbar N_k} \sum_{\mathbf{k}\alpha \beta \sigma} i \sum_{\mathbf{r}_{i\alpha}} \mathbf{r}_{i\alpha} t_{i\alpha, j\beta} e^{i\mathbf{k}r_{i\alpha}} c_{\mathbf{k}\alpha}^\dagger c_{\mathbf{k}\beta} = \frac{e}{\hbar N_k} \sum_{\mathbf{k}\alpha \beta \sigma} \nabla_{\mathbf{k}} h(\mathbf{k})_{\alpha\beta} c_{\mathbf{k}\alpha}^\dagger c_{\mathbf{k}\beta} := \frac{e}{N_k} \sum_{\mathbf{k}\alpha \beta \sigma} \mathbf{v}_{\alpha\beta} c_{\mathbf{k}\alpha}^\dagger c_{\mathbf{k}\beta} \quad (2.83)$$

This means current density is

$$\mathbf{j}_{\mathbf{q}} = \langle \hat{\mathbf{j}} \rangle_{\mathbf{q}} = \frac{e}{N_k} \sum_{\mathbf{k}\alpha \beta \sigma} \mathbf{v}_{\alpha\beta}(\mathbf{k}) \langle c_{\mathbf{k}\alpha\sigma}^\dagger c_{\mathbf{k}\beta\sigma} \rangle_{\mathbf{q}} = \frac{2e}{N_k} \sum_{\mathbf{k}\alpha \beta} \mathbf{v}_{\alpha\beta}(\mathbf{k}) \langle c_{\mathbf{k}\alpha\uparrow}^\dagger c_{\mathbf{k}\beta\uparrow} \rangle_{\mathbf{q}}, \quad (2.84)$$

which can be expressed using the BdG energies

$$\mathbf{j}_{\mathbf{q}} = \frac{2e}{N_k} \sum_{\mathbf{k}\alpha \beta n} \mathbf{v}_{\alpha\beta}(\mathbf{k}) [U_{\mathbf{q}\mathbf{k}}]_{\alpha n} [U_{\mathbf{q}\mathbf{k}}^*]_{\beta n} n_F(E_n), \quad (2.85)$$

where $n \in \{1, \dots, 2N_{\text{orb}}\}$.

2.3 Dynamical Mean-Field Theory

The foundational idea of Dynamical Mean Field Theory (DMFT) is to map the full interacting problem to the problem of a single lattice site (or a small cluster of lattice sites) embedded in a mean field encompassing all non-local correlation effects. This mapping can be seen in fig. 2.3. In contrast to static mean-field theories such as BCS theory, DMFT treats all local correlations. When the interaction strength becomes comparable to the kinetic energy of the electrons, the electrons are becoming increasingly localized and the band structure picture is not applicable anymore. One hallmark effect in this strongly-correlated regime is the interaction driven metal-insulator (Mott) transition. Using DMFT, the Mott transition seen in materials like V_2O_3 [56] can be explained in the Hubbard model [57].

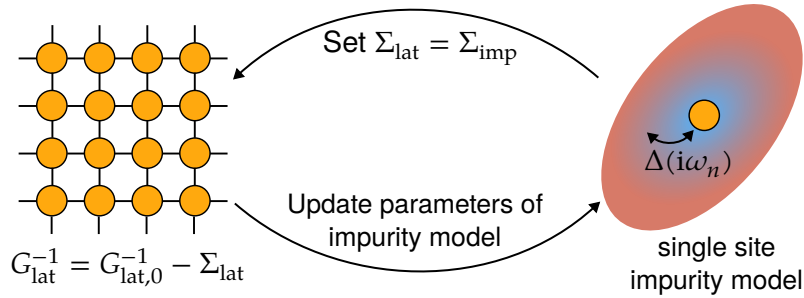


Figure 2.3 – Mapping of the full lattice problem onto a single-site impurity model. This also visualizes the DMFT self-consistency loop: Coming from the full lattice problem, an impurity model is set up, which is then solved to get the self-energy Σ_{imp} , which encompasses all interaction effects. The loop is converged when $\Sigma_{\text{lat}} = \Sigma_{\text{imp}}$, otherwise the impurity self-energy is a new guess for the self-energy of the lattice problem.

In this section I will describe the Green's function formalism, the mapping of the lattice problem onto the impurity problem and the resulting self-consistency loop of DMFT. Additionally, I will also describe how to treat the superconducting state in terms of Green's function and the consequences for the DMFT self-consistency condition. I will not fully derive the equations of DMFT here, for a more expansive introduction see refs. [27, 29, 58, 59].

Green's Function Formalism

Green's functions are a method to encode influence of many-body effects on propagation of particles in a system. Depending on the context different kinds of Green's functions are employed. Matsubara Green's functions naturally includes finite temperatures, which is done via a Wick rotation of the time variable t into imaginary time

$$t \rightarrow -i\tau \quad (2.86)$$

where τ is real and has the dimension time. This enables the simultaneous expansion of exponential $e^{-\beta H}$ coming from the thermodynamic average and e^{-iHt} coming from the time evolution of operators. Matsubara Greens function are defined as

$$G_{\alpha_1 \alpha_2}(\tau_1, \tau_2) = -\langle T_\tau(c_{\alpha_1}(\tau_1)c_{\alpha_2}^\dagger(\tau_2)) \rangle \quad (2.87)$$

with:

- $c_\alpha, c_\alpha^\dagger$ fermionic creation/annihilation operators of quantum states α in the Heisenberg time-evolution picture $\hat{A}(\tau) = e^{\tau H} \hat{A} e^{-\tau H}$
- $\langle \cdot \rangle = \text{Tr}(\hat{\rho} \cdot)$ the thermal expectation value with statistical operator $\hat{\rho} = e^{-\beta H}/Z$ with partition function Z and Hamiltonian H
- Time-ordering operator

$$\begin{aligned} T_\tau(A(\tau)B(\tau')) &= \Theta(\tau - \tau')A(\tau)B(\tau') \pm \Theta(\tau' - \tau)B(\tau')A(\tau) \\ &= \begin{cases} A(\tau)B(\tau') & \text{if } \tau < \tau' \\ B(\tau')A(\tau) & \text{if } \tau' < \tau \end{cases} \end{aligned} \quad (2.88)$$

In thermal equilibrium, the Green's function only depends on time differences $\tau_1 - \tau_2$, so by defining $\tau = \tau_1 - \tau_2$, one can work with a single time.

Fermionic Matsubara Green's functions are antiperiodic in time with periodicity β . For $-\beta < 0 < 0$, the cyclic properties of the trace means that

$$G(\tau) = -G(\tau + \beta). \quad (2.89)$$

This means that the Green's functions can be restricted to the interval $0 < \tau < \beta$ and in turn, there is a Fourier expansion with discrete frequencies $\omega_n = (2n+1)\pi/\beta$:

$$G(i\omega_n) = \int_0^\beta d\tau G(\tau) e^{i\omega_n \tau} \quad (2.90)$$

$$G(\tau) = \frac{1}{\beta} \sum_n G(i\omega_n) e^{-i\omega_n \tau}. \quad (2.91)$$

In lattice system there is a spatial dependence $\alpha = \mathbf{R}$ and due to translational invariance, G only depends on $\mathbf{R}_1 - \mathbf{R}_2$. This means one can transform between real-space and crystal momentum representation as

$$G(\mathbf{k}) = \sum_i G(\mathbf{R}_i) e^{i\mathbf{k}\mathbf{R}_i} \quad (2.92)$$

$$G(\mathbf{r}) = \frac{1}{N_{\mathbf{k}}} \sum_{\mathbf{k}} G(\mathbf{k}) e^{-i\mathbf{k}\mathbf{r}}, \quad (2.93)$$

both in τ and Matsubara frequency space.

Matsubara Green's function make calculations computationally easier, but do not give information on experimental observables. This can be done by extending the description to real frequencies ω by analytic continuation [29]

$$G^R(\omega + i\eta) = G(i\omega_n \rightarrow \omega + i\eta), \quad (2.94)$$

where the $\eta > 0$ is an infinitesimal part. On real frequencies, the retarded Green's function G^R connects to experimentally measurable quantities, such as the spectral function

$$A(\omega, \mathbf{k}) = -\frac{1}{\pi} \Im(G(\omega + i\eta, \mathbf{k})), \quad (2.95)$$

describing the excitation spectrum of the system being measured.

Dyson Equation

A non-interacting system with dispersion $\epsilon_{\mathbf{k}}$ can be described by the free Green's function

$$G_0(i\omega_n, \mathbf{k}) = [i\omega_n - \epsilon_{\mathbf{k}}]^{(-1)} \quad (2.96)$$

The feedback of the environment on propagation of the particle is encoded in an object called the self-energy $\Sigma(i\omega_n, \mathbf{k})$. The interacting and non-interacting Green's function are connected by the Dyson equation

$$G = G_0 + G_0 \Sigma G. \quad (2.97)$$

The solution to the Dyson equation can formally be written as

$$G(i\omega_n, \mathbf{k}) = [G_0(i\omega_n, \mathbf{k}) - \Sigma(\mathbf{k}, i\omega_n)]^{-1}. \quad (2.98)$$

The real part of $\Sigma(\mathbf{k}, i\omega_n)$ describes renormalization of energy levels and the imaginary part describes the finite lifetime of quasiparticles.

The self-energy enables a systematic inclusion of interaction effects and approximations given certain system restraints. In DMFT, the self-energy is taken to be purely local, which is exact in the limit of infinite dimension, but it can still capture effects which depend significantly on local dynamic correlations in low-dimensional system.

Mapping to Impurity Model and DMFT Self-Consistency Loop

The central idea of DMFT is to map the full lattice problem onto a problem of a single impurity of the form

$$H_{\text{IM}} = H_{\text{imp}} + H_{\text{bath}} + H_{\text{hyb}} \quad (2.99)$$

with the terms

$$H_{\text{imp}} = \sum_{\alpha\sigma} \epsilon_{d,\alpha} d_{\alpha\sigma}^\dagger d_{\alpha\sigma} + \sum_{\alpha} U_{\alpha} n_{d,\alpha\uparrow} n_{d,\alpha\downarrow} \quad (2.100)$$

$$H_{\text{bath}} = \sum_{\mathbf{k},n\sigma} \epsilon_{\mathbf{k},n} c_{\mathbf{k}n\sigma}^\dagger c_{\mathbf{k}n\sigma} \quad (2.101)$$

$$H_{\text{hyb}} = \sum_{\mathbf{k},\alpha n\sigma} V_{\mathbf{k},\alpha n} d_{\alpha\sigma}^\dagger c_{\mathbf{k}n\sigma} + V_{\mathbf{k},\alpha n}^* c_{\mathbf{k}n\sigma}^\dagger d_{\alpha\sigma} \quad (2.102)$$

Here, d are the operators for the impurity site and c are the operators for the bath, which is characterized by the energy levels $\epsilon_{\mathbf{k},n}$ and hybridization to the impurity orbitals $V_{\mathbf{k},\alpha n}$.

Using the path-integral formalism, the bath degrees of freedom can be integrated out [59]:

$$S_{\text{imp}} = - \int_0^\beta d\tau d\tau' \sum_{\alpha\beta,\sigma} d_{\alpha\sigma}^*(\tau) [G_{\text{imp},0}^{-1}]_{\alpha\beta}(\tau - \tau') d_{\beta\sigma}(\tau') \quad (2.103)$$

$$+ \int_0^\beta d\tau \sum_{\alpha} U_{\alpha} n_{d,\alpha\uparrow} n_{d,\alpha\downarrow} \quad (2.104)$$

with the non-interacting impurity Green's function $G_{\text{imp},0}$, given by

$$[G_{\text{imp},0}]_{\alpha,\beta} = \left[i\omega_n - \epsilon_{d,\alpha} - \sum_{\mathbf{k}} \frac{V_{\mathbf{k},\alpha n}^* V_{\mathbf{k},n\beta}}{i\omega_n - \epsilon_{\mathbf{k},n}} \right] \quad (2.105)$$

The approximation of DMFT lies in the fact that the self-energy of the impurity model $\Sigma_{\text{imp}}(i\omega_n)$ is purely local, where the lattice self-energy $\Sigma_{\text{lat}}(i\omega_n, \mathbf{k})$ carries a \mathbf{k} -dependence. As shown in the illustration fig. 2.3, these two quantities are set equal to go from the impurity to the lattice model:

$$\Sigma_{\text{lat}}(i\omega_n, \mathbf{k}) \approx \Sigma_{\text{imp}}(i\omega_n) =: \Sigma(i\omega_n). \quad (2.106)$$

Using this, the local lattice Greens function is obtained by summing over the \mathbf{k} -dependence:

$$G_{\text{loc}}(i\omega_n) = \frac{1}{N_k} \sum_{\mathbf{k}} [i\omega_n - h(\mathbf{k}) - \Sigma(i\omega_n)]^{-1} \stackrel{!}{=} G_{\text{imp}}(i\omega_n). \quad (2.107)$$

By demanding that this is equal to the impurity Green's function G_{imp} , the mapping to the impurity model is defined. Using the Dyson equation, the non-interacting Greens function for the impurity problem can be calculated as

$$G_{\text{imp},0}(i\omega_n) = [G_{\text{loc}}^{-1}(i\omega_n) + \Sigma(i\omega_n)]^{-1}. \quad (2.108)$$

This sets up an impurity model which can be solved by computational means.

Given a solution to the impurity problem has been found, this interacting Green's function $G_{\text{imp}}(i\omega_n)$ can be used to calculate the self-energy via

$$\Sigma(i\omega_n) = G_{\text{imp},0}^{-1}(i\omega_n) - G_{\text{imp}}^{-1}(i\omega_n). \quad (2.109)$$

The DMFT self-consistency loop as shown in fig. 2.3 consists of the following steps:

1. Choose an initial self-energy Σ , for example $\Sigma = 0$.
2. Use eq. (2.107) to calculate $G_{\text{loc}}(i\omega_n)$.
3. Calculate the non-interacting impurity Green's function from eq. (2.108).
4. Solve the interacting impurity model, obtaining $G_{\text{imp}}(i\omega_n)$.
5. Calculate a new self-energy $\Sigma(i\omega_n)$ via eq. (2.109).
6. Check convergence of the self-energy (or alternatively via the condition $G_{\text{loc}}(i\omega_n) = G_{\text{imp}}(i\omega_n)$). Otherwise, use this self-energy as a new input in step 2.

Step 4, solving the impurity model is the computationally hardest step in the DMFT loop and many different solver methods have been developed over the years with differing use cases, accuracy and numerical demands.

The TRIQS toolkit [60] implements methods to work with Green's functions, using different impurity solvers to enable efficient development of DMFT methods. For the calculations in this thesis, Exact Diagonalization (ED) as

implemented in the EDIpack library [61] has been used. It was made available to TRIQS via a compatibility layer by I. Krivenko and L. Crippa [62].

The idea of ED as introduced by Caffarel and Krauth [63] is to represent the bath with a finite number of discrete bath sites N_b . This means the Hamiltonian for the impurity model is adjusted to

$$H_{\text{bath}} = \sum_{\substack{k \in \{1, \dots, N_b\} \\ n\sigma}} \epsilon_{k,n} c_{kn\sigma}^\dagger c_{kn\sigma} \quad (2.110)$$

$$H_{\text{hyb}} = \sum_{\substack{k \in \{1, \dots, N_b\} \\ \alpha n\sigma}} V_{k,\alpha n} d_{\alpha\sigma}^\dagger c_{kn\sigma} + V_{k,n\alpha} c_{kn\sigma}^\dagger d_{\alpha\sigma} \quad (2.111)$$

In ED, one needs to fit the bath parameters $\{\epsilon_k, V_k\}$ to optimally represent the lattice system, i.e. find the best fit to approximate the hybridization function $\Delta(i\omega_n)$ of the impurity model by the discrete hybridization function

$$\Delta_{\{\epsilon_k, V_k\}}(i\omega_n) = \sum_{k=1}^{N_b} \frac{|V_k|^2}{i\omega_n - \epsilon_k} \quad (2.112)$$

containing only a finite amount of poles. This is implemented in EDIpack.

Nambu-Gorkov Green's Functions

To describe superconductivity in the Green's function formalism, one introduces the Nambu-Gor'kov formalism [59]. Using the Nambu spinors as in eq. (2.59)

$$\Psi_{\mathbf{k},\mathbf{q},\alpha} = \begin{pmatrix} c_{\mathbf{k}\alpha\uparrow} & c_{\mathbf{q}-\mathbf{k}\alpha\downarrow}^\dagger \end{pmatrix}^T, \quad (2.113)$$

the Green's functions become 2×2 matrices in Nambu space

$$[\mathcal{G}_{\mathbf{q}}(\tau, \mathbf{k})]_{\alpha\gamma} = -\langle T_\tau \Psi_{\mathbf{k},\mathbf{q},\alpha} \Psi_{\mathbf{k},\mathbf{q},\gamma}^\dagger \rangle \quad (2.114)$$

$$= \begin{pmatrix} -\langle T_\tau c_{\mathbf{k},\alpha,\uparrow} c_{\mathbf{k},\gamma,\uparrow}^\dagger \rangle & -\langle T_\tau c_{\mathbf{k},\alpha,\uparrow} c_{\mathbf{q}-\mathbf{k},\gamma,\downarrow} \rangle \\ -\langle T_\tau c_{\mathbf{q}-\mathbf{k},\alpha,\downarrow}^\dagger c_{\mathbf{k},\gamma,\uparrow} \rangle & -\langle T_\tau c_{\mathbf{q}-\mathbf{k},\alpha,\downarrow} c_{\mathbf{q}-\mathbf{k},\gamma,\downarrow}^\dagger \rangle \end{pmatrix} \quad (2.115)$$

$$= \begin{pmatrix} [\mathcal{G}_{\mathbf{q}}^{\downarrow\downarrow}(\tau, \mathbf{k})]_{\alpha\gamma} & [\mathcal{G}_{\mathbf{q}}^{\uparrow\downarrow}(\tau, \mathbf{k})]_{\alpha\gamma} \\ [\mathcal{G}_{\mathbf{q}}^{\downarrow\downarrow}(\tau, \mathbf{k})]_{\alpha\gamma} & [\mathcal{G}_{\mathbf{q}}^{\uparrow\downarrow}(\tau, \mathbf{k})]_{\alpha\gamma} \end{pmatrix}. \quad (2.116)$$

Due to the definition of the Nambu spinors with \mathbf{q} only appearing in the spin-down sector, only $\mathcal{G}^{\downarrow\downarrow}$ carries the \mathbf{q} -dependence. The superconducting state is

marked by the fact that the so-called anomalous Green's functions $\mathcal{G}^{\uparrow\downarrow}, \mathcal{G}^{\downarrow\uparrow}$ are non-zero. On Matsubara frequencies, the Nambu-Gor'kov Green's functions is set up via

$$\begin{aligned} & [\mathcal{G}_{\mathbf{q}}(i\omega_n, \mathbf{k})]^{-1} \\ &= \begin{pmatrix} (i\omega_n + \mu) - h(\mathbf{k}) - \Sigma^N(i\omega_n) & -\Sigma^{AN}(i\omega_n) \\ -\Sigma^{AN}(i\omega_n) & (i\omega_n - \mu) + h(-\mathbf{k} + \mathbf{q}) + (\Sigma^N)^*(i\omega_n) \end{pmatrix} \end{aligned} \quad (2.117)$$

with the self-energy now being composed of a normal and anomalous part:

$$\mathcal{S}(i\omega_n) = \begin{pmatrix} \Sigma^N(i\omega_n) & \Sigma^{AN}(i\omega_n) \\ \Sigma^{AN}(i\omega_n) & -(\Sigma^N)^*(i\omega_n) \end{pmatrix} \quad (2.118)$$

The self-consistency cycle of DMFT introduced in the section above can equivalently be defined in Nambu space, replacing eqs. (2.107) to (2.109):

$$\begin{cases} \mathcal{G}_{loc}(i\omega_n) = \frac{1}{N_k} \sum_{\mathbf{k}} \mathcal{G}(i\omega_n, \mathbf{k}) \\ \mathcal{G}_{imp,0} = [\mathcal{G}_{loc}^{-1}(i\omega_n) + \mathcal{S}(i\omega_n)]^{-1} \\ \mathcal{S}(i\omega_n) = \mathcal{G}_{imp,0}^{-1}(i\omega_n) - \mathcal{G}_{imp}^{-1}(i\omega_n) \end{cases} \quad (2.119)$$

2.4 Quantum Geometry

Topic in quantum materials: quantum geometry and its influence on a many (quantum) material properties [34]. First (?) example: the Integer quantum Hall effect [64] that was explained by Thouless et al. to be a consequence of the unique topology of the ground state of the electron [65].

Concept of quantum geometry first formulated in 1980 by Provost and Vallee [66].

Parameter dependent Hamiltonian $\{H(\lambda)\}$, smooth dependence on parameter $\lambda = (\lambda_1, \lambda_2, \dots) \in \mathcal{M}$ (base manifold)

Hamiltonian acts on parametrized Hilbert space $\mathcal{H}(\lambda)$

Eigenenergies $E_n(\lambda)$, eigenstates $|\phi_n(\lambda)\rangle$

System state $|\psi(\lambda)\rangle$ is linear combination of $|\psi_n(\lambda)\rangle$ at every point in \mathcal{M}

Infinitesimal variation of the parameter $d\lambda$:

$$ds^2 = \|\psi(\lambda + d\lambda) - \psi(\lambda)\|^2 = \langle \delta\psi | \delta\psi \rangle = \langle \partial_\mu \psi | \partial_\nu \psi \rangle d\lambda^\mu d\lambda^\nu = (\gamma_{\mu\nu} + i\sigma_{\mu\nu}) d\lambda^\mu d\lambda^\nu \quad (2.120)$$

Last part is splitting up into real and imaginary part

Recently, the Quantum Geometric Tensor (and in turn the quantum metric) was measured [67].

Quantum Metric and Superfluid Weight

Write up notes about quantum metric and superfluid weight

3

Decorated Graphene Model

Following the 2018 discovery of superconductivity in twisted bilayer Graphene [16], graphene-based systems gained a renewed interest as a platform for strongly correlated physics. Two methods to engineer strong electron correlations emerged: twisted multilayer systems [16–20] and multilayer systems without twisting, such as Bernal bilayer, ABC or ABCA layered systems [21]. Through different means, electrons in these systems become localized so that interaction effects get more strongly pronounced. Connecting both kind of systems is the strong quantum geometry coming from the Graphene Dirac cones [22], which plays a role in stabilizing superconducting [17, 23] and magnetic order [24, 25].

Witt et al. suggested another platform for strongly correlated physics based on Graphene with the same strong quantum geometry, but higher intrinsic energy scales and thus also higher critical temperatures for strong correlation phenomena [68]. The model is inspired by an earlier experiment [69] of a SiC(0001) substrate with a single layer of Graphene on top and Sn as an intercalant¹ between the substrate and the Graphene layer. The system shows signs of Mott-Hubbard bands, a hallmark of strong correlation physics. Witt et al. suggested that by using different group-IV intercalants (C, Si, Ge, Sn, Pb) between the graphene sheet and the semiconducting SiC(0001) substrate, different distances to the Graphene sheet occur in the ground state. Band structures obtained from Density Functional Theory (DFT) show a relatively flat band at the Fermi level from the intercalant's p_z orbitals hybridized to the Dirac bands of graphene for all intercalants, with the hybridization strength being tuned by the equilibrium distance of the Graphene sheet and the intercalants.

In this thesis I will be treating an elemental model introduced in the work by Witt et al. capturing the essential flat band character of the system. The lattice structure can be seen in fig. 3.1. It consists of the usual hexagonal Graphene lattice, with an additional atom at one of the sublattice sites providing the flat band. Here, the hopping V models the hybridization

¹An intercalant is an atom or molecule inserted between the layers of layered system.

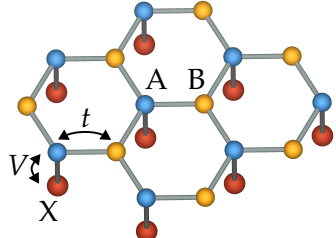


Figure 3.1 – Lattice structure of decorated graphene honeycomb lattice. with impurity X hybridized to sublattice site A. Only hopping t between sublattices A and B as well as V between X and A exist. Created using VESTA [70].

This elemental model shows two symmetry distinct Mott states for the small and large V regimes: in the low V regime, the X are responsible for the development of local moments and Mottness occurs at, where in the high V limit, the B atom are responsible. Between these Mott states emerges a metallic state, similar to the topological phase transition of non-interacting bands in the Su-Schrieffer-Heeger model [71].

In twisted or untwisted multilayer Graphene systems, the energy scale for the emergence of ordered phases is $\mathcal{O}(\text{meV})$, corresponding to temperatures of a few K [72, 73]. In contrast, the energy scale in this decorated Graphene model is set by the hopping t , i.e. $\mathcal{O}(\text{eV})$ for Graphene, so that the correlated flat band physics might persist to higher temperatures.

3.1 Lattice Structure

Monolayer graphene forms a honeycomb lattice [74], which is a hexagonal Bravais lattice with a two-atom basis, as can be seen in fig. 3.2a. The primitive lattice vectors of the hexagonal lattice are:

$$\mathbf{a}_1 = \frac{a}{2} \begin{pmatrix} 1 \\ \sqrt{3} \end{pmatrix}, \quad \mathbf{a}_2 = \frac{a}{2} \begin{pmatrix} 1 \\ -\sqrt{3} \end{pmatrix} \quad (3.1)$$

with lattice constant $a = \sqrt{3}a_0 \approx 2.46 \text{ \AA}$, using the nearest-neighbor distance a_0 . The vectors from atom A to the nearest-neighbor atoms B_i ($i = 1, 2, 3$) are

$$\delta_{AB,1} = \begin{pmatrix} 0 \\ \frac{a}{\sqrt{3}} \end{pmatrix}, \quad \delta_{AB,2} = \begin{pmatrix} \frac{a}{2} \\ -\frac{a}{2\sqrt{3}} \end{pmatrix}, \quad \delta_{AB,3} = \begin{pmatrix} -\frac{a}{2} \\ -\frac{a}{2\sqrt{3}} \end{pmatrix} \quad (3.2)$$

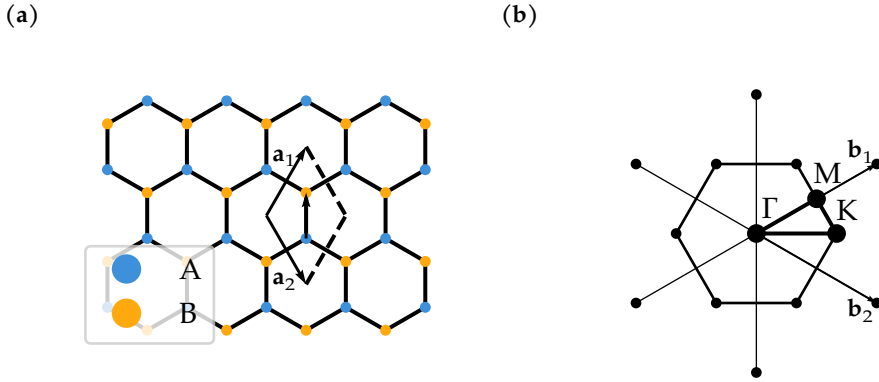


Figure 3.2 – (a) Graphene lattice structure with primitive lattice vectors $\mathbf{a}_1, \mathbf{a}_2$ and (b) Brillouin zone with reciprocal vectors $\mathbf{b}_1, \mathbf{b}_2$. Both images created with lattpy [75]

and the vectors from atom B to the nearest-neighbor atoms A_i ($i = 1, 2, 3,$) are

$$\delta_{BA,1} = \begin{pmatrix} 0 \\ -\frac{a}{\sqrt{3}} \end{pmatrix}, \quad \delta_{BA,2} = \begin{pmatrix} -\frac{a}{2} \\ \frac{a}{2\sqrt{3}} \end{pmatrix}, \quad \delta_{BA,3} = \begin{pmatrix} \frac{a}{2} \\ \frac{a}{2\sqrt{3}} \end{pmatrix}. \quad (3.3)$$

The primitive reciprocal lattice vectors $\mathbf{b}_1, \mathbf{b}_2$ fulfill:

$$\mathbf{a}_1 \cdot \mathbf{b}_1 = \mathbf{a}_2 \cdot \mathbf{b}_2 = 2\pi \quad (3.4)$$

$$\mathbf{a}_1 \cdot \mathbf{b}_2 = \mathbf{a}_2 \cdot \mathbf{b}_1 = 0, \quad (3.5)$$

so that

$$\mathbf{b}_1 = \frac{2\pi}{a} \begin{pmatrix} 1 \\ \frac{1}{\sqrt{3}} \end{pmatrix}, \quad \mathbf{b}_2 = \frac{2\pi}{a} \begin{pmatrix} 1 \\ -\frac{1}{\sqrt{3}} \end{pmatrix}. \quad (3.6)$$

The first Brillouin zone of the hexagonal lattice is shown in fig. 3.2b, with the points of high symmetry

$$\Gamma = \begin{pmatrix} 0 \\ 0 \end{pmatrix}, \quad M = \frac{\pi}{a} \begin{pmatrix} 1 \\ \frac{1}{\sqrt{3}} \end{pmatrix}, \quad K = \frac{4\pi}{3a} \begin{pmatrix} 1 \\ 0 \end{pmatrix}. \quad (3.7)$$

The elemental model as shown in fig. 3.1 has the following kinetic terms:

$$H_0 = -t \sum_{\langle ij \rangle, \sigma} c_{i,\sigma}^{(A),\dagger} c_{j,\sigma}^{(B)} + V \sum_{i,\sigma\sigma'} d_{i,\sigma}^\dagger c_{i,\sigma'}^{(A)} + \text{h.c.} \quad (3.8)$$

with

- d - operators on the X atom
- $c^{(\epsilon)}$ - operators on the graphene sites ($\epsilon = A, B$)
- t - nearest neighbor hopping between Graphene sites
- V - hopping between X and Graphene A sites.

Using the Fourier transformation

$$c_{i\alpha\sigma} = \frac{1}{\sqrt{N}} \sum_{\mathbf{k}} e^{i\mathbf{k}\mathbf{r}_{i\alpha}} c_{\mathbf{k}\alpha\sigma}, \quad (3.9)$$

the hopping term becomes

$$-t \sum_{\langle ij \rangle, \sigma} c_{i,\sigma}^{(A),\dagger} c_{j,\sigma}^{(B)} \quad (3.10)$$

$$= -t \sum_{i, \delta_{AB}, \sigma} c_{i,\sigma}^{(A)\dagger} c_{i+\delta_{AB}, \sigma}^{(B)} \quad (3.11)$$

$$= -\frac{t}{N^2} \sum_{i,\sigma} \sum_{\mathbf{k}, \mathbf{k}', \delta_{AB}} (e^{-i\mathbf{k}\mathbf{r}_{i\alpha}} c_{\mathbf{k},\sigma}^{(A)\dagger}) (e^{i\mathbf{k}'\mathbf{r}_{i\alpha} + \delta_{AB}} c_{\mathbf{k}',\sigma}^{(B)}) \quad (3.12)$$

$$= -\frac{t}{N^2} \sum_{\mathbf{k}, \mathbf{k}', \delta_{AB}, \sigma} c_{\mathbf{k},\sigma}^{(A)\dagger} c_{\mathbf{k}',\sigma}^{(B)} e^{i\mathbf{k}'\delta_{AB}} e^{i(\mathbf{k}(\delta_A - \delta_B) + \mathbf{k}'(\delta_A - \delta_B))} \sum_i e^{-i\mathbf{k}\mathbf{R}_i} e^{i\mathbf{k}'\mathbf{R}_i} \quad (3.13)$$

$$= -\frac{t}{N^2} \sum_{\mathbf{k}, \mathbf{k}', \sigma} c_{\mathbf{k},\sigma}^{(A)\dagger} c_{\mathbf{k}',\sigma}^{(B)} \sum_{\delta_{AB}} e^{i\mathbf{k}'\delta_{AB}} e^{i(\mathbf{k}(\delta_A - \delta_B) + \mathbf{k}'(\delta_A - \delta_B))} (N^2 \delta_{\mathbf{k}, \mathbf{k}'}) \quad (3.14)$$

$$= -t \sum_{\mathbf{k}, \sigma} c_{\mathbf{k},\sigma}^{(A)\dagger} c_{\mathbf{k},\sigma}^{(B)} \sum_{\delta_{AB}} e^{i(\mathbf{k}\delta_{AB} + 2k_y a)} = \sum_{\mathbf{k}, \sigma} f_{\mathbf{k}} c_{\mathbf{k},\sigma}^{(A)\dagger} c_{\mathbf{k},\sigma}^{(B)}. \quad (3.15)$$

The factor $f_{\mathbf{k}}$ can be written out explicitly using the nearest-neighbor vectors, for example

$$\mathbf{k} \cdot \delta_{AB,1} = \begin{pmatrix} k_x \\ k_y \end{pmatrix} \cdot \begin{pmatrix} 0 \\ \frac{a}{\sqrt{3}} \end{pmatrix} = \frac{1}{\sqrt{3}} k_y. \quad (3.16)$$

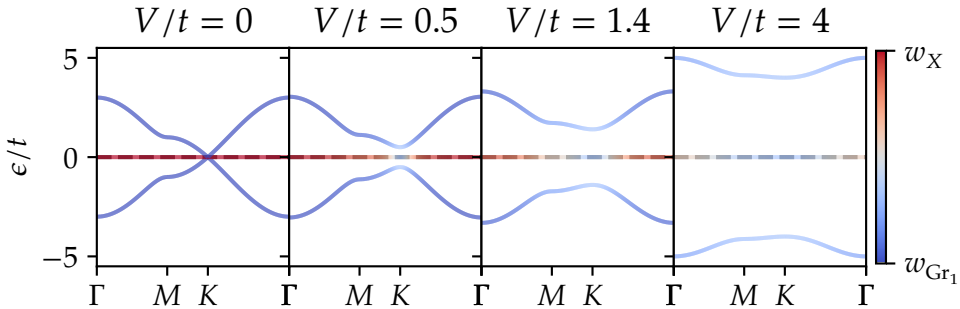


Figure 3.3 – Bands of the non-interacting decorated Graphene model

This gives:

$$f_{\mathbf{k}} = -t \sum_{\delta_{AB}} e^{i(\mathbf{k}\delta_{AB} + 2k_y a)} \quad (3.17)$$

$$= -t_{\text{Gr}} e^{2ik_y a} \left(e^{\frac{i}{\sqrt{3}}k_y} + e^{\frac{i-a}{2\sqrt{3}}(\sqrt{3}k_x - k_y)} + e^{\frac{i-a}{2\sqrt{3}}(-\sqrt{3}k_x - k_y)} \right) \quad (3.18)$$

$$= -t_{\text{Gr}} e^{2ik_y a} \left(e^{\frac{i}{\sqrt{3}}k_y} + 2e^{-\frac{i}{2\sqrt{3}}k_y} \cos\left(\frac{a}{2}k_x\right) \right). \quad (3.19)$$

Using the fact that $\delta_{BA,i} = -\delta_{AB,i}$, it follows

$$-t \sum_{\delta_{BA}} e^{i\mathbf{k}\delta_{BA}} = -t \sum_{\delta_{AB}} e^{-i\mathbf{k}\delta_{AB}} = \left(-t \sum_{\delta_{AB}} e^{i\mathbf{k}\delta_{AB}} \right)^* = f_{\mathbf{k}}^*, \quad (3.20)$$

which then gives

$$H_0 = \sum_{\mathbf{k},\sigma} C_{\mathbf{k},\sigma}^\dagger \begin{pmatrix} 0 & f_{\mathbf{k}} & V \\ f_{\mathbf{k}}^* & 0 & 0 \\ V & 0 & 0 \end{pmatrix} C_{\mathbf{k},\sigma} \quad (3.21)$$

$$C_{\mathbf{k},\sigma} = (c_{\mathbf{k},\sigma}^{A,\dagger} \ c_{\mathbf{k},\sigma}^{B,\dagger} \ d_{\mathbf{k},\sigma}^\dagger)^T \quad (3.22)$$

The band structure for the non-interacting decorated graphene model is obtained by diagonalizing the matrix in eq. (3.21).

Write more about the bands
Derivative of h(k)

3.2 Quantum Geometry

Section about quantum geometry, maybe with lattice site local quantum metric?

Application of the Finite-Momentum Method

4.1 Decorated Graphene Model

Critical Temperatures

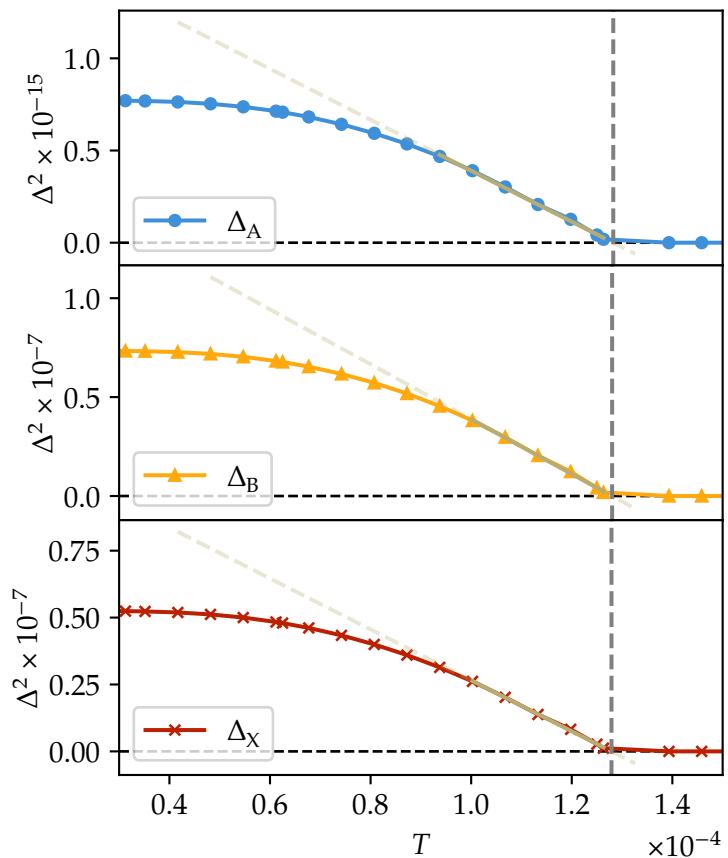


Figure 4.1 – Linear fit for extracting the critical temperature

Critical temperatures via eq. (2.9):

$$|\Psi|^2 \propto T_C - T. \quad (4.1)$$

Fit and corresponding T_C are shown in fig. 4.1. Notable:

- the gaps Δ_α have very different orders of magnitude, but fall in the same way, i.e. have the same critical temperature

Can plot critical temperatures against V and U .

Figure 4.2 shows T_C and gaps against V .

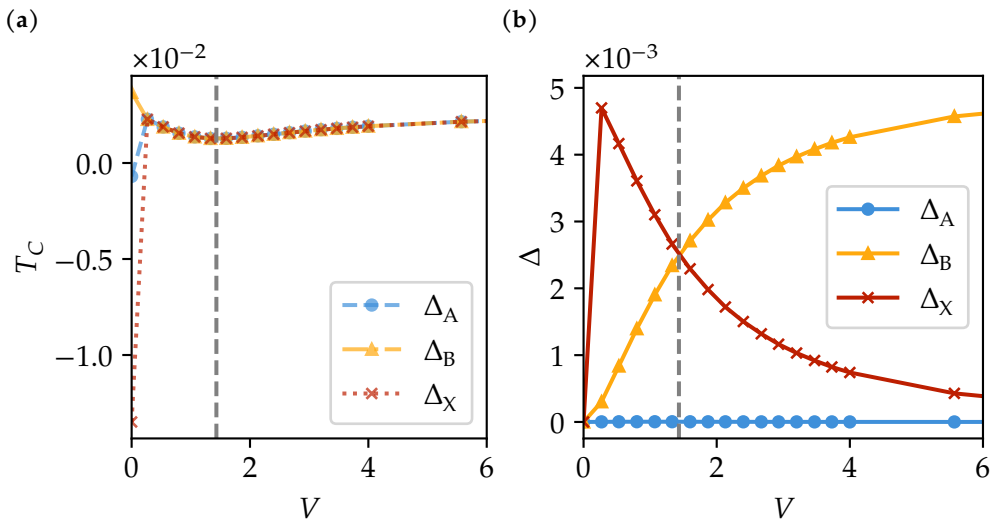


Figure 4.2 – T (a) Critical temperatures vs V . (b) Gaps vs V .

Notable:

- Minimum of T_C and gaps at some $V = 1.43$, corresponds with metallic V in repulsive Hubbard model
- But no gap closure
- T_C follows maximal gap
- What is happening at $V = 0$? New jobs

This

Figure 4.3 shows T_C and gaps against U .

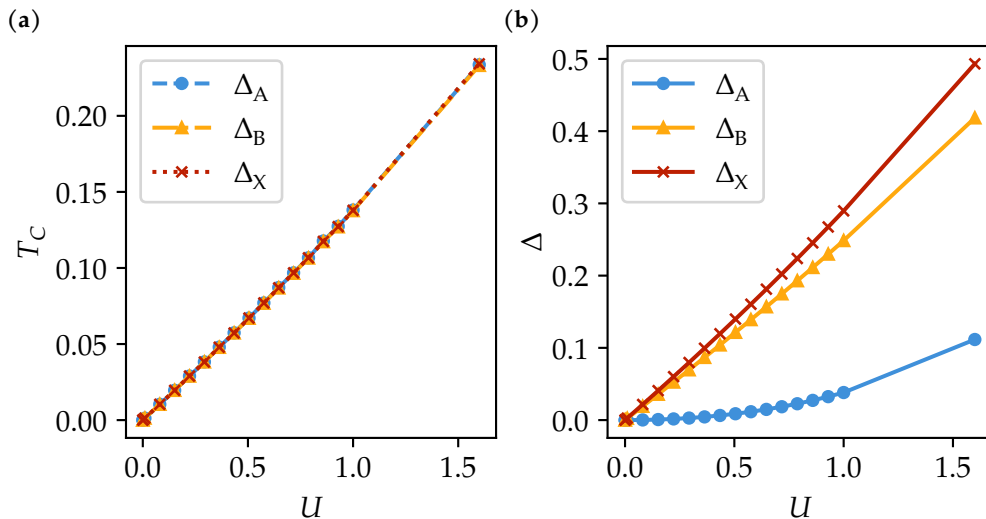


Figure 4.3 – T (a) Critical temperatures vs U. (b) Gaps vs U.

Notable:

- Linear with interaction strength, typical for flat band in BCS (reference)
- Exponential for Graphene A band

Figure 4.4 shows T_C and gaps against U for different V .

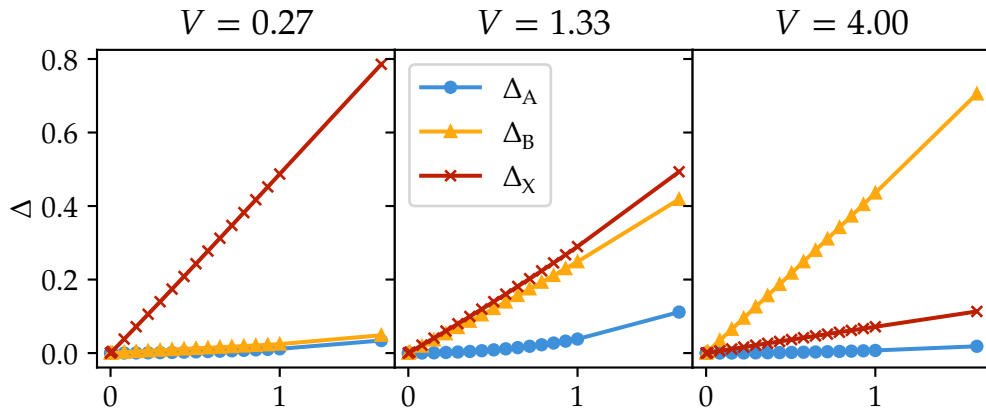


Figure 4.4 – Gaps vs U. for different V

Notable:

- Low V: flat band on X, high V: flat band on Graphene B, medium V: both
- mirrors the switchover seen in the gaps against V and the band structure

Extracting the Superconducting Length Scales

Plot two important gaps against q in fig. 4.5 for a medium V

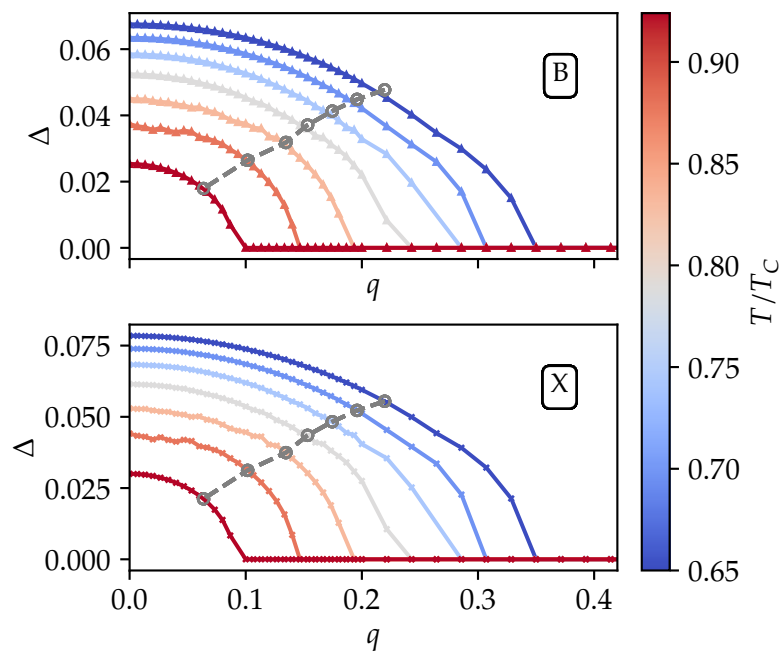
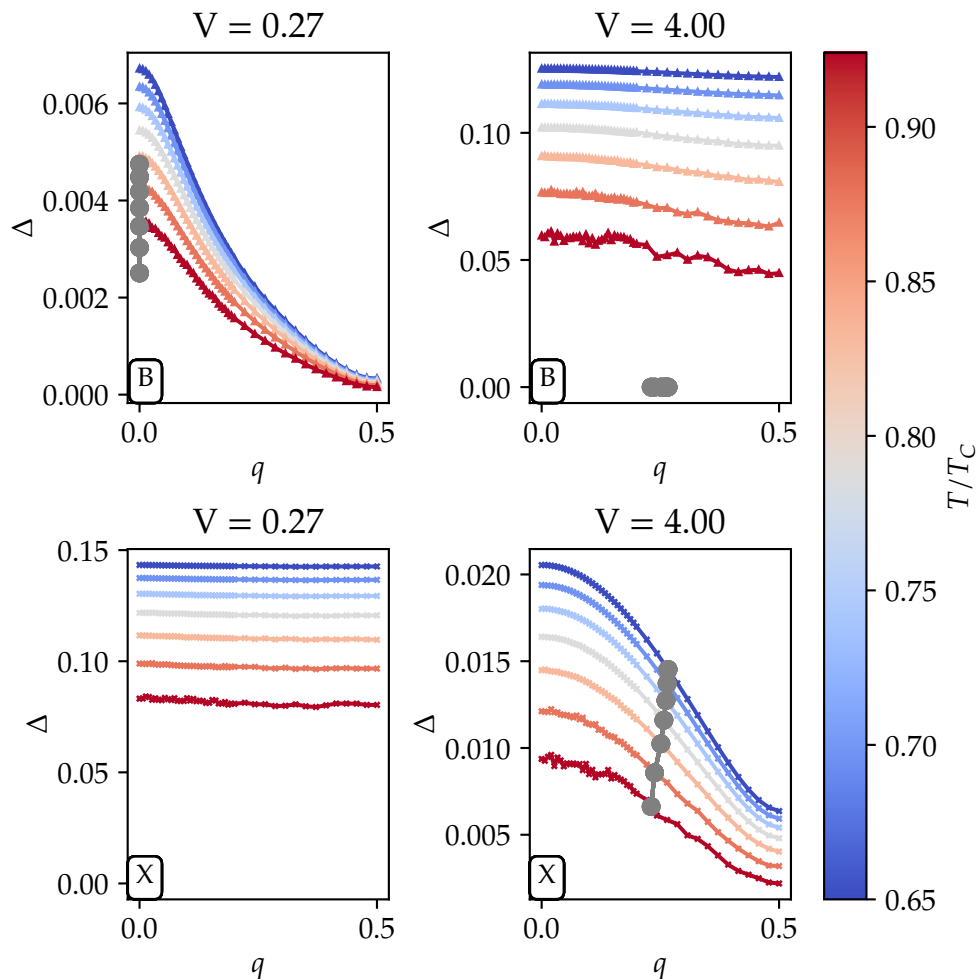


Figure 4.5 – Gap vs q

Notable:

- Plot two important gaps against q in fig. 4.6 for a high and low V

Notable things in plot

Figure 4.6 – Gap vs q

Notable:

-

Take

$$\xi(T) = \frac{1}{\sqrt{2}|\mathbf{Q}|} \quad (4.2)$$

with \mathbf{Q} such that

$$\left| \frac{\psi_{\mathbf{Q}}(T)}{\psi_0(T)} \right| = \frac{1}{\sqrt{2}} \quad (4.3)$$

Plot also current against q fig. 4.7

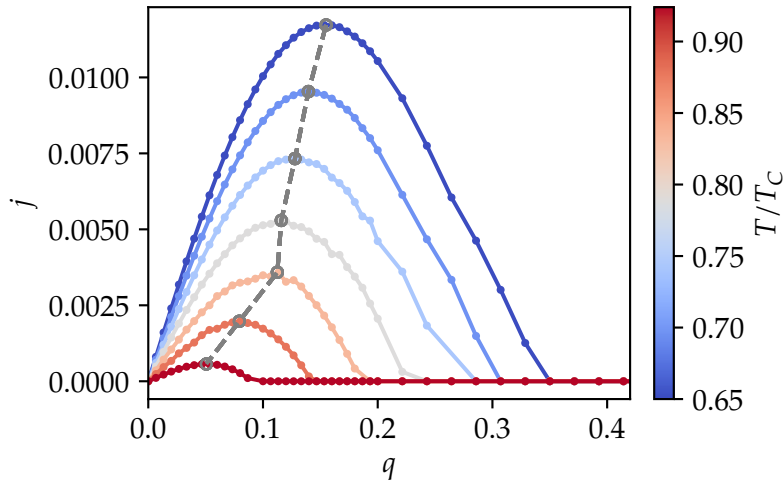


Figure 4.7 – Current against q

Notable:

-

Calculate $\xi(T)$ and $\lambda_L(T)$. Plot against T and fit to get $\xi_0, \lambda_{L,0}$.

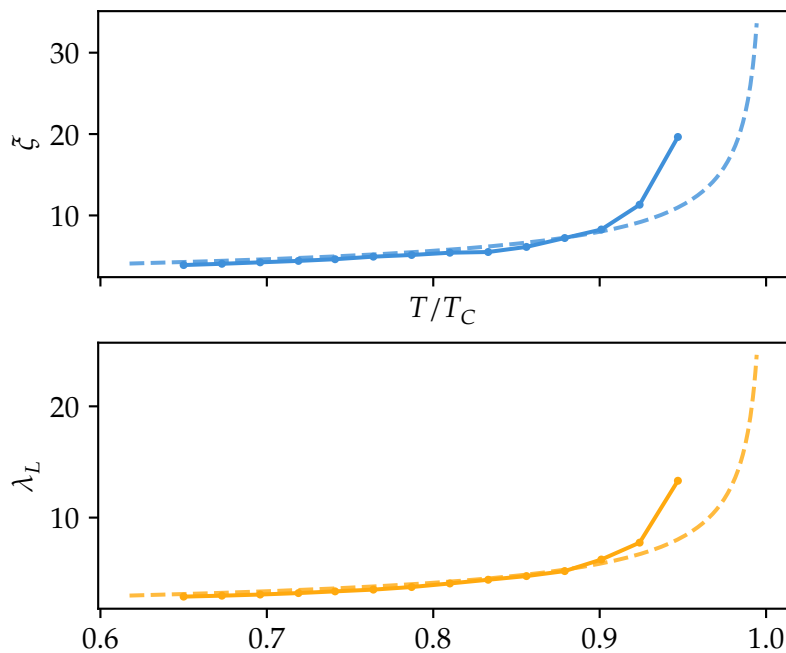


Figure 4.8 – Temperature fits for ξ and λ_L

Length Scales

Plot SC length scales vs V or vs U? between different gaps?

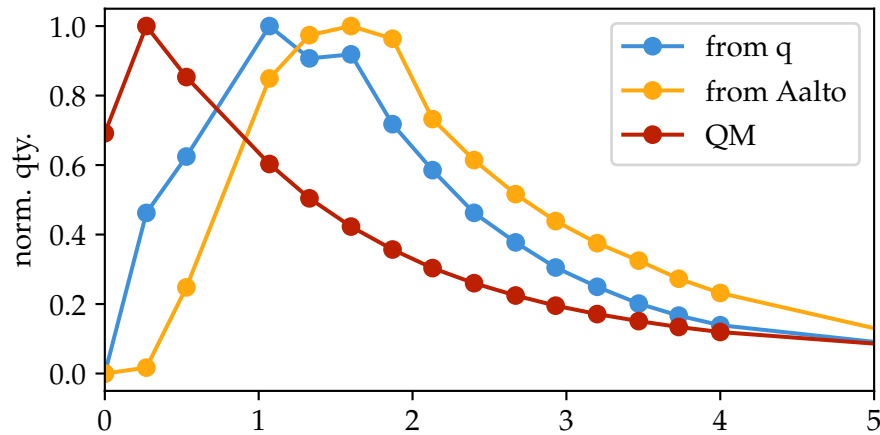


Figure 4.9 – DS

4.2 One-Band Hubbard Model on the Square Lattice

Can extract T_C same way as above. Plot it against U .

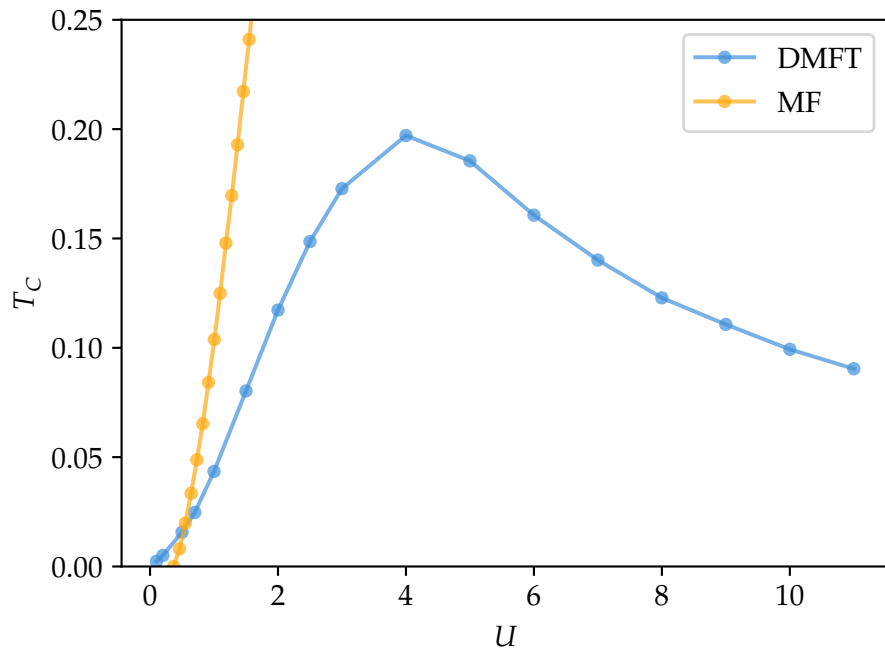


Figure 4.10 – T_C against U (also mean field results)

Notable:

-

Extracting Superconducting Length Scales

Extraction same as before, plot gap and current against q in section 4.2.

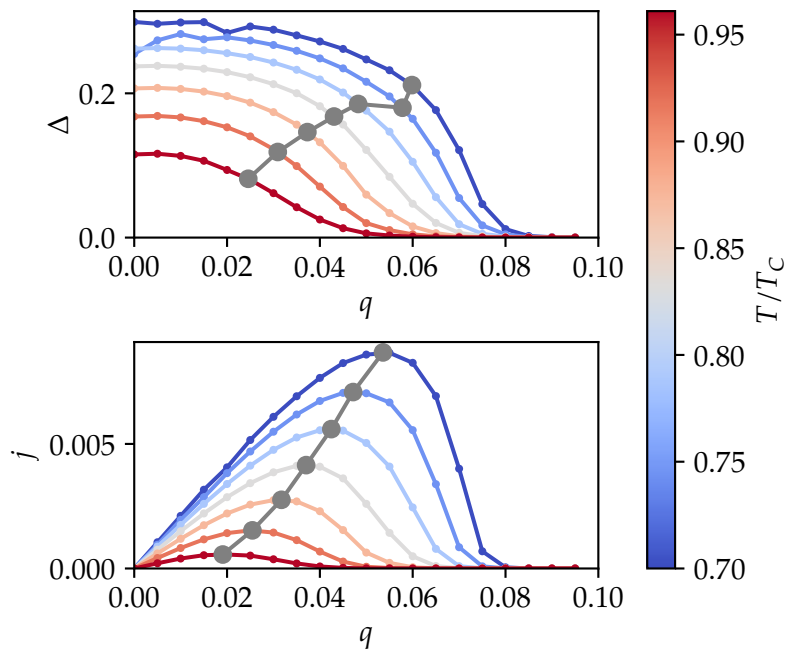


Figure 4.11 – Gap and current vs q .

Notable:

-

Calculate $\xi(T)$ and $\lambda_L(T)$. Plot against T and fit to get $\xi_0, \lambda_{L,0}$.

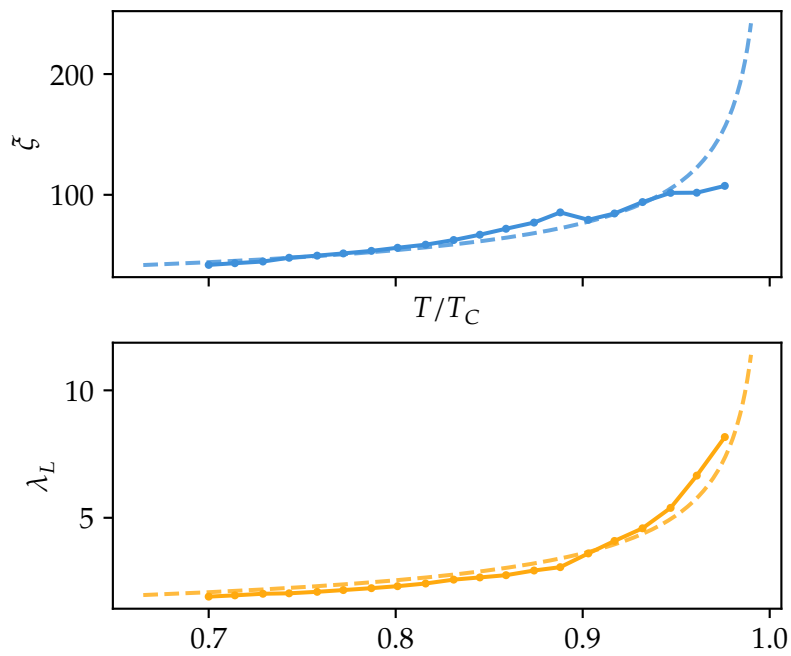


Figure 4.12 – Temperature fits for ξ and λ_L

BCS-BEC Crossover

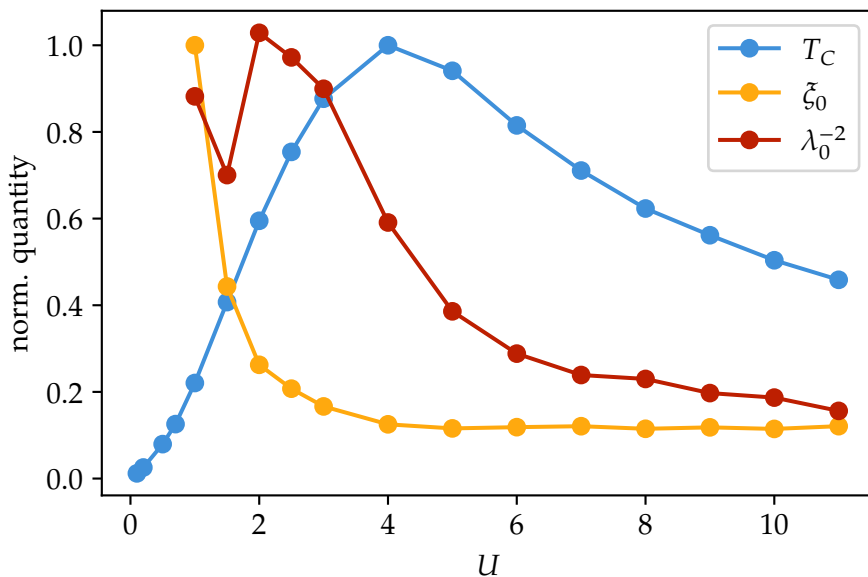


Figure 4.13 – Normalized TC/xi/DS against U (to show BCS-BEC crossover)

Comparison of MF and DMFT Data

- Plot MF and DMFT xi and lambda against U
- Plot DS from Aalto formula vs MF and DMFT DS

Conclusion

5

Other Methods to Extract Superconducting Length Scales

A

Computational Implementation and Data Availability

B

BCS code

The implementation of BCS self-consistency with finite momentum was done by me from ground-up. The code and documentation is available at github.com/Ruberhauptmann/quantmet. The implementation relies on the work of many contributors of packages in Python's ecosystem, most important among them NumPy [76], SciPy [77], Matplotlib [78], Pandas [79, 80] and Parasweep [81].

Units:

$$E = t \quad (\text{B.1})$$

$$l = a \quad (\text{B.2})$$

$$\hbar = 1 \quad (\text{B.3})$$

$$k_B = 1 \quad (\text{B.4})$$

$$\mu_0 = 1 \quad (\text{B.5})$$

$$\lambda_L = \sqrt{\frac{2}{3\sqrt{3}\xi j_{dp}}} \quad (\text{B.6})$$

For units of q :

$$q = x|b_1| = x \frac{4\pi}{\sqrt{3}a} \quad (\text{B.7})$$

$$\lambda_L = \frac{1}{q} = \frac{\sqrt{3}}{4x\pi}a \quad (\text{B.8})$$

All the data and instructions on how to reproduce the calculations and analysis is available at osf.io/sajeh/. For reproducibility, Datalad [82] is used.

Plots: color sequences by Petroff [83].

DMFT

DMFT loop using TRIQS [60], it can also be found under osf.io/sajeh/.

Bibliography

- [1] United Nations. *International Year of Quantum Science and Technology, 2025*. May 10, 2024. [url: https://docs.un.org/A/78/L.70](https://docs.un.org/A/78/L.70) (visited on 02/18/2025) (cit. on p. 1).
- [2] H.-L. Huang et al. "Superconducting Quantum Computing: A Review". In: *Science China Information Sciences* 63.8 (July 15, 2020), p. 180501. issn: 1869-1919. doi: 10.1007/s11432-020-2881-9 (cit. on p. 1).
- [3] F. Arute et al. "Quantum Supremacy Using a Programmable Superconducting Processor". In: *Nature* 574.7779 (Oct. 2019), pp. 505–510. issn: 1476-4687. doi: 10.1038/s41586-019-1666-5 (cit. on p. 1).
- [4] B. D. Josephson. "Possible New Effects in Superconductive Tunnelling". In: *Physics Letters* 1.7 (July 1, 1962), pp. 251–253. issn: 0031-9163. doi: 10.1016/0031-9163(62)91369-0 (cit. on p. 1).
- [5] M. I. Faley et al. "High-Tc SQUID Biomagnetometers". In: *Superconductor Science and Technology* 30.8 (July 2017), p. 083001. issn: 0953-2048. doi: 10.1088/1361-6668/aa73ad (cit. on p. 1).
- [6] A. M. Klushin et al. "Present and Future of High-Temperature Superconductor Quantum-Based Voltage Standards". In: *IEEE Instrumentation & Measurement Magazine* 23.2 (Apr. 2020), pp. 4–12. issn: 1941-0123. doi: 10.1109/MIM.2020.9062678 (cit. on p. 1).
- [7] H. K. Onnes. "Further Experiments with Liquid Helium. G. On the Electrical Resistance of Pure Metals, Etc. VI. On the Sudden Change in the Rate at Which the Resistance of Mercury Disappears." In: *Through Measurement to Knowledge: The Selected Papers of Heike Kamerlingh Onnes 1853–1926*. Ed. by K. Gavroglu and Y. Goudaroulis. Dordrecht: Springer Netherlands, 1991, pp. 267–272. isbn: 978-94-009-2079-8. doi: 10.1007/978-94-009-2079-8_17 (cit. on p. 1).
- [8] W. Meissner and R. Ochsenfeld. "Ein neuer Effekt bei Eintritt der Supraleitfähigkeit". In: *Naturwissenschaften* 21.44 (Nov. 1, 1933), pp. 787–788. issn: 1432-1904. doi: 10.1007/BF01504252 (cit. on p. 1).

-
- [9] J. G. Bednorz and K. A. Müller. "Possible High Tc Superconductivity in the Ba–La–Cu–O System". In: *Zeitschrift für Physik B Condensed Matter* 64.2 (June 1, 1986), pp. 189–193. issn: 1431-584X. doi: 10.1007/BF01303701 (cit. on p. 1).
 - [10] S.-i. Uchida et al. "High Tc Superconductivity of La-Ba-Cu Oxides". In: *Japanese Journal of Applied Physics* 26 (1A Jan. 1, 1987), p. L1. issn: 1347-4065. doi: 10.1143/JJAP.26.L1 (cit. on p. 1).
 - [11] D. Rybicki et al. "Perspective on the Phase Diagram of Cuprate High-Temperature Superconductors". In: *Nature Communications* 7.1 (May 6, 2016), p. 11413. issn: 2041-1723. doi: 10.1038/ncomms11413 (cit. on p. 1).
 - [12] P. A. Rinck. *Magnetic Resonance in Medicine - A Critical Introduction*. isbn: 978-628-01-2260-1. url: <http://www.magnetic-resonance.org/> (cit. on p. 2).
 - [13] F. Schmidt et al. "Operation Experience and Further Development of a High-Temperature Superconducting Power Cable in the Long Island Power Authority Grid". In: *Physics Procedia*. SUPERCONDUCTIVITY CENTENNIAL Conference 2011 36 (Jan. 1, 2012), pp. 1137–1144. issn: 1875-3892. doi: 10.1016/j.phpro.2012.06.190 (cit. on p. 2).
 - [14] K. Konstantopoulou et al. "Design Optimization and Evaluation of the 3 kA MgB₂ Cable at 4.3 K for the Superconducting Link Project at CERN". In: *Supercond. Sci. Technol.* 32.8 (2019), p. 085003. doi: 10.1088/1361-6668/ab13e7 (cit. on p. 2).
 - [15] Q. Chen et al. "When Superconductivity Crosses over: From BCS to BEC". In: *Reviews of Modern Physics* 96.2 (May 23, 2024), p. 025002. doi: 10.1103/RevModPhys.96.025002 (cit. on pp. 2, 3).
 - [16] Y. Cao et al. "Unconventional Superconductivity in Magic-Angle Graphene Superlattices". In: *Nature* 556.7699 (Apr. 2018), pp. 43–50. issn: 1476-4687. doi: 10.1038/nature26160 (cit. on pp. 3, 4, 30).
 - [17] M. Tanaka et al. "Superfluid Stiffness of Magic-Angle Twisted Bilayer Graphene". In: *Nature* 638.8049 (Feb. 2025), pp. 99–105. issn: 1476-4687. doi: 10.1038/s41586-024-08494-7 (cit. on pp. 3, 30).

-
- [18] P. Törmä, S. Peotta, and B. A. Bernevig. "Superconductivity, Superfluidity and Quantum Geometry in Twisted Multilayer Systems". In: *Nature Reviews Physics* 4.8 (Aug. 2022), pp. 528–542. issn: 2522-5820. doi: 10.1038/s42254-022-00466-y (cit. on pp. 3, 30).
 - [19] E. Y. Andrei and A. H. MacDonald. "Graphene Bilayers with a Twist". In: *Nature Materials* 19.12 (Dec. 2020), pp. 1265–1275. issn: 1476-4660. doi: 10.1038/s41563-020-00840-0 (cit. on pp. 3, 30).
 - [20] F. Xie et al. "Topology-Bounded Superfluid Weight in Twisted Bilayer Graphene". In: *Physical Review Letters* 124.16 (Apr. 24, 2020), p. 167002. doi: 10.1103/PhysRevLett.124.167002 (cit. on pp. 3, 30).
 - [21] P. A. Pantaleón et al. "Superconductivity and Correlated Phases in Non-Twisted Bilayer and Trilayer Graphene". In: *Nature Reviews Physics* 5.5 (May 2023), pp. 304–315. issn: 2522-5820. doi: 10.1038/s42254-023-00575-2 (cit. on pp. 3, 30).
 - [22] T. Wehling, A. Black-Schaffer, and A. Balatsky. "Dirac Materials". In: *Advances in Physics* 63.1 (Jan. 2, 2014), pp. 1–76. issn: 0001-8732. doi: 10.1080/00018732.2014.927109 (cit. on pp. 3, 30).
 - [23] L. Liang et al. "Band Geometry, Berry Curvature, and Superfluid Weight". In: *Physical Review B* 95.2 (Jan. 27, 2017), p. 024515. doi: 10.1103/PhysRevB.95.024515 (cit. on pp. 3, 13, 30).
 - [24] A. Abouelkomsan, K. Yang, and E. J. Bergholtz. "Quantum Metric Induced Phases in Moiré Materials". In: *Physical Review Research* 5.1 (Feb. 10, 2023), p. L012015. doi: 10.1103/PhysRevResearch.5.L012015 (cit. on pp. 3, 30).
 - [25] J. Liu and X. Dai. "Orbital Magnetic States in Moiré Graphene Systems". In: *Nature Reviews Physics* 3.5 (May 2021), pp. 367–382. issn: 2522-5820. doi: 10.1038/s42254-021-00297-3 (cit. on pp. 3, 30).
 - [26] B. Keimer and J. E. Moore. "The Physics of Quantum Materials". In: *Nature Physics* 13.11 (Nov. 2017), pp. 1045–1055. issn: 1745-2481. doi: 10.1038/nphys4302 (cit. on p. 5).
 - [27] P. Coleman. *Introduction to Many-Body Physics*. Cambridge University Press, Nov. 2015. isbn: 978-0-521-86488-6. doi: 10.1017/CBO9781139020916 (cit. on pp. 5, 15, 22).

-
- [28] M. Tinkham. *Introduction to Superconductivity*. 2. ed. International Series in Pure and Applied Physics. New York: McGraw-Hill, 1996. 454 pp. ISBN: 978-0-07-064878-4 (cit. on pp. 5, 13, 15).
 - [29] H. Bruus and K. Flensberg. *Many-Body Quantum Theory in Condensed Matter Physics: An Introduction*. Oxford Graduate Texts. Oxford, New York: Oxford University Press, Nov. 11, 2004. 466 pp. ISBN: 978-0-19-856633-5 (cit. on pp. 5, 22, 24).
 - [30] A. I. Larkin and A. A. Varlamov. *Theory of Fluctuations in Superconductors*. Oxford Science Publications 127. Oxford Oxford: Clarendon Press Oxford University Press, 2005. ISBN: 978-0-19-852815-9 (cit. on p. 5).
 - [31] K. H. Bennemann and J. B. Ketterson, eds. *Superconductivity*. Berlin, Heidelberg: Springer Berlin Heidelberg, 2008. ISBN: 978-3-540-73252-5. doi: 10.1007/978-3-540-73253-2 (cit. on p. 5).
 - [32] N. Witt et al. "Bypassing the Lattice BCS–BEC Crossover in Strongly Correlated Superconductors through Multiorbital Physics". In: *npj Quantum Materials* 9.1 (Dec. 10, 2024), pp. 1–10. ISSN: 2397-4648. doi: 10.1038/s41535-024-00706-7 (cit. on pp. 5, 12).
 - [33] S. Peotta and P. Törmä. "Superfluidity in Topologically Nontrivial Flat Bands". In: *Nature Communications* 6.1 (Nov. 20, 2015), p. 8944. ISSN: 2041-1723. doi: 10.1038/ncomms9944 (cit. on pp. 5, 13, 18).
 - [34] J. Yu et al. *Quantum Geometry in Quantum Materials*. Dec. 30, 2024. doi: 10.48550/arXiv.2501.00098. Pre-published (cit. on pp. 5, 28).
 - [35] E. Noether. "Invariante Variationsprobleme". In: *Nachrichten von der Gesellschaft der Wissenschaften zu Göttingen, Mathematisch-Physikalische Klasse* 1918 (1918), pp. 235–257. URL: <https://eudml.org/doc/59024> (visited on 12/10/2024) (cit. on p. 6).
 - [36] L. D. Landau. "On the Theory of Phase Transitions". In: *Zhurnal Eksperimental'noi i Teoreticheskoi Fiziki* 7 (1937). Ed. by D. ter Haar, pp. 19–32. doi: 10.1016/B978-0-08-010586-4.50034-1 (cit. on p. 6).
 - [37] V. L. Ginzburg and L. D. Landau. "On the Theory of Superconductivity". In: *Zhurnal Eksperimental'noi i Teoreticheskoi Fiziki* 20 (1950). Ed. by D. ter Haar, pp. 1064–1082. doi: 10.1016/b978-0-08-010586-4.50078-x (cit. on pp. 6, 8).

-
- [38] A. Q. Chen et al. "Finite Momentum Cooper Pairing in Three-Dimensional Topological Insulator Josephson Junctions". In: *Nature Communications* 9.1 (Aug. 28, 2018), p. 3478. issn: 2041-1723. doi: 10.1038/s41467-018-05993-w (cit. on p. 12).
 - [39] P. Wan et al. "Orbital Fulde–Ferrell–Larkin–Ovchinnikov State in an Ising Superconductor". In: *Nature* 619.7968 (July 2023), pp. 46–51. issn: 1476-4687. doi: 10.1038/s41586-023-05967-z (cit. on p. 12).
 - [40] N. F. Q. Yuan and L. Fu. "Supercurrent Diode Effect and Finite-Momentum Superconductors". In: *Proceedings of the National Academy of Sciences* 119.15 (Apr. 12, 2022), e2119548119. doi: 10.1073/pnas.2119548119 (cit. on p. 12).
 - [41] J. J. Kinnunen et al. "The Fulde–Ferrell–Larkin–Ovchinnikov State for Ultracold Fermions in Lattice and Harmonic Potentials: A Review". In: *Reports on Progress in Physics* 81.4 (Feb. 2018), p. 046401. issn: 0034-4885. doi: 10.1088/1361-6633/aaa4ad (cit. on pp. 12, 17).
 - [42] J. Bardeen. "Critical Fields and Currents in Superconductors". In: *Reviews of Modern Physics* 34.4 (Oct. 1, 1962), pp. 667–681. doi: 10.1103/RevModPhys.34.667 (cit. on p. 13).
 - [43] K. Xu, P. Cao, and J. R. Heath. "Achieving the Theoretical Depairing Current Limit in Superconducting Nanomesh Films". In: *Nano Letters* 10.10 (Oct. 13, 2010), pp. 4206–4210. issn: 1530-6984. doi: 10.1021/nl102584j (cit. on p. 13).
 - [44] J. Bardeen, L. N. Cooper, and J. R. Schrieffer. "Theory of Superconductivity". In: *Physical Review* 108.5 (Dec. 1, 1957), pp. 1175–1204. doi: 10.1103/PhysRev.108.1175 (cit. on p. 14).
 - [45] L. C. Hebel and C. P. Slichter. "Nuclear Relaxation in Superconducting Aluminum". In: *Physical Review* 107.3 (Aug. 1, 1957), pp. 901–902. doi: 10.1103/PhysRev.107.901 (cit. on p. 15).
 - [46] L. C. Hebel and C. P. Slichter. "Nuclear Spin Relaxation in Normal and Superconducting Aluminum". In: *Physical Review* 113.6 (Mar. 15, 1959), pp. 1504–1519. doi: 10.1103/PhysRev.113.1504 (cit. on p. 15).
 - [47] I. Giaever and K. Megerle. "Study of Superconductors by Electron Tunneling". In: *Physical Review* 122.4 (May 15, 1961), pp. 1101–1111. doi: 10.1103/PhysRev.122.1101 (cit. on p. 15).

-
- [48] F. London. "A New Conception of Supraconductivity". In: *Nature* 140.3549 (Nov. 1, 1937), pp. 793–796. issn: 1476-4687. doi: 10.1038/140793a0 (cit. on p. 15).
 - [49] X. Zhou et al. "High-Temperature Superconductivity". In: *Nature Reviews Physics* 3.7 (July 2021), pp. 462–465. issn: 2522-5820. doi: 10.1038/s42254-021-00324-3 (cit. on p. 15).
 - [50] J. Hubbard and B. H. Flowers. "Electron Correlations in Narrow Energy Bands". In: *Proceedings of the Royal Society of London. Series A. Mathematical and Physical Sciences* 276.1365 (Nov. 26, 1963), pp. 238–257. doi: 10.1098/rspa.1963.0204 (cit. on p. 15).
 - [51] J. Kanamori. "Electron Correlation and Ferromagnetism of Transition Metals". In: *Progress of Theoretical Physics* 30.3 (Sept. 1, 1963), pp. 275–289. issn: 0033-068X. doi: 10.1143/PTP.30.275 (cit. on p. 15).
 - [52] M. C. Gutzwiller. "Effect of Correlation on the Ferromagnetism of Transition Metals". In: *Physical Review Letters* 10.5 (Mar. 1, 1963), pp. 159–162. doi: 10.1103/PhysRevLett.10.159 (cit. on p. 15).
 - [53] F. C. Zhang and T. M. Rice. "Effective Hamiltonian for the Superconducting Cu Oxides". In: *Physical Review B* 37.7 (Mar. 1, 1988), pp. 3759–3761. doi: 10.1103/PhysRevB.37.3759 (cit. on p. 15).
 - [54] M. Qin et al. "The Hubbard Model: A Computational Perspective". In: *Annual Review of Condensed Matter Physics* 13 (Volume 13, 2022 Mar. 10, 2022), pp. 275–302. issn: 1947-5454, 1947-5462. doi: 10.1146/annurev-conmatphys-090921-033948 (cit. on p. 16).
 - [55] R. Micnas, J. Ranninger, and S. Robaszkiewicz. "Superconductivity in Narrow-Band Systems with Local Nonretarded Attractive Interactions". In: *Reviews of Modern Physics* 62.1 (Jan. 1, 1990), pp. 113–171. doi: 10.1103/RevModPhys.62.113 (cit. on p. 16).
 - [56] D. B. McWhan, T. M. Rice, and J. P. Remeika. "Mott Transition in Cr-Doped V₂O₃". In: *Physical Review Letters* 23.24 (Dec. 15, 1969), pp. 1384–1387. issn: 0031-9007. doi: 10.1103/PhysRevLett.23.1384 (cit. on p. 21).

-
- [57] M. J. Rozenberg, G. Kotliar, and X. Y. Zhang. "Mott-Hubbard Transition in Infinite Dimensions. II". In: *Physical Review B* 49.15 (Apr. 15, 1994), pp. 10181–10193. issn: 0163-1829, 1095-3795. doi: 10.1103/PhysRevB.49.10181 (cit. on p. 21).
 - [58] E. Pavarini et al., eds. *Dynamical Mean-Field Theory of Correlated Electrons*. Schriften Des Forschungszentrums Jülich Reihe Modeling and Simulation Band/volume 12. Jülich: Forschungszentrum Jülich, Zentralbibliothek, Verlag, 2022. 1 p. isbn: 978-3-95806-619-9 (cit. on p. 22).
 - [59] A. Georges et al. "Dynamical Mean-Field Theory of Strongly Correlated Fermion Systems and the Limit of Infinite Dimensions". In: *Reviews of Modern Physics* 68.1 (Jan. 1, 1996), pp. 13–125. doi: 10.1103/RevModPhys.68.13 (cit. on pp. 22, 25, 27).
 - [60] O. Parcollet et al. "TRIQS: A Toolbox for Research on Interacting Quantum Systems". In: *Computer Physics Communications* 196 (Nov. 1, 2015), pp. 398–415. issn: 0010-4655. doi: 10.1016/j.cpc.2015.04.023 (cit. on pp. 26, 53).
 - [61] A. Amaricci et al. "EDIpak: A Parallel Exact Diagonalization Package for Quantum Impurity Problems". In: *Computer Physics Communications* 273 (Apr. 1, 2022), p. 108261. issn: 0010-4655. doi: 10.1016/j.cpc.2021.108261 (cit. on p. 27).
 - [62] I. Krivenko. *Krivenko/Edipack2triqs*. Mar. 10, 2025. url: <https://github.com/krivenko/edipack2triqs> (visited on 03/11/2025) (cit. on p. 27).
 - [63] M. Caffarel and W. Krauth. "Exact Diagonalization Approach to Correlated Fermions in Infinite Dimensions: Mott Transition and Superconductivity". In: *Physical Review Letters* 72.10 (Mar. 7, 1994), pp. 1545–1548. doi: 10.1103/PhysRevLett.72.1545 (cit. on p. 27).
 - [64] K. v. Klitzing, G. Dorda, and M. Pepper. "New Method for High-Accuracy Determination of the Fine-Structure Constant Based on Quantized Hall Resistance". In: *Physical Review Letters* 45.6 (Aug. 11, 1980), pp. 494–497. doi: 10.1103/PhysRevLett.45.494 (cit. on p. 28).
 - [65] D. J. Thouless et al. "Quantized Hall Conductance in a Two-Dimensional Periodic Potential". In: *Physical Review Letters* 49.6 (Aug. 9, 1982), pp. 405–408. doi: 10.1103/PhysRevLett.49.405 (cit. on p. 28).

-
- [66] J. P. Provost and G. Vallee. "Riemannian Structure on Manifolds of Quantum States". In: *Communications in Mathematical Physics* 76.3 (Sept. 1, 1980), pp. 289–301. issn: 1432-0916. doi: 10.1007/BF02193559 (cit. on p. 28).
 - [67] M. Kang et al. "Measurements of the Quantum Geometric Tensor in Solids". In: *Nature Physics* 21.1 (Jan. 2025), pp. 110–117. issn: 1745-2481. doi: 10.1038/s41567-024-02678-8 (cit. on p. 29).
 - [68] N. Witt et al. *Quantum Geometry and Local Moment Swapover in Correlated Graphene Heterostructures*. Mar. 5, 2025. doi: 10.48550/arXiv.2503.03700. Pre-published (cit. on p. 30).
 - [69] C. Ghosal et al. *Electronic Correlations in Epitaxial Graphene: Mott States Proximitized to a Relativistic Electron Gas*. Dec. 2, 2024. doi: 10.48550/arXiv.2412.01329. Pre-published (cit. on p. 30).
 - [70] K. Momma and F. Izumi. "VESTA 3 for Three-Dimensional Visualization of Crystal, Volumetric and Morphology Data". In: *Journal of Applied Crystallography* 44.6 (Dec. 1, 2011), pp. 1272–1276. issn: 0021-8898. doi: 10.1107/S0021889811038970 (cit. on p. 31).
 - [71] W. P. Su, J. R. Schrieffer, and A. J. Heeger. "Soliton Excitations in Polyacetylene". In: *Physical Review B* 22.4 (Aug. 15, 1980), pp. 2099–2111. doi: 10.1103/PhysRevB.22.2099 (cit. on p. 31).
 - [72] K. P. Nuckolls and A. Yazdani. "A Microscopic Perspective on Moiré Materials". In: *Nature Reviews Materials* 9.7 (July 2024), pp. 460–480. issn: 2058-8437. doi: 10.1038/s41578-024-00682-1 (cit. on p. 31).
 - [73] P. A. Pantaleón et al. "Superconductivity and Correlated Phases in Non-Twisted Bilayer and Trilayer Graphene". In: *Nature Reviews Physics* 5.5 (May 2023), pp. 304–315. issn: 2522-5820. doi: 10.1038/s42254-023-00575-2 (cit. on p. 31).
 - [74] G. Yang et al. "Structure of Graphene and Its Disorders: A Review". In: *Science and Technology of Advanced Materials* 19.1 (Aug. 29, 2018), pp. 613–648. issn: 1468-6996. doi: 10.1080/14686996.2018.1494493 (cit. on p. 31).
 - [75] D. Jones. *Lattpy*. May 2022. url: <https://github.com/dylanljones/lattpy> (cit. on p. 32).

-
- [76] C. R. Harris et al. "Array Programming with NumPy". In: *Nature* 585.7825 (Sept. 2020), pp. 357–362. issn: 1476-4687. doi: 10.1038/s41586-020-2649-2 (cit. on p. 52).
 - [77] P. Virtanen et al. "SciPy 1.0: Fundamental Algorithms for Scientific Computing in Python". In: *Nature Methods* 17.3 (Mar. 2020), pp. 261–272. issn: 1548-7105. doi: 10.1038/s41592-019-0686-2 (cit. on p. 52).
 - [78] J. D. Hunter. "Matplotlib: A 2D Graphics Environment". In: *Computing in Science & Engineering* 9.3 (May 2007), pp. 90–95. issn: 1558-366X. doi: 10.1109/MCSE.2007.55 (cit. on p. 52).
 - [79] W. McKinney. "Data Structures for Statistical Computing in Python". In: Python in Science Conference. Austin, Texas, 2010, pp. 56–61. doi: 10.25080/Majora-92bf1922-00a (cit. on p. 52).
 - [80] T. pandas development team. *Pandas-Dev/Pandas: Pandas*. Version v2.2.3. Zenodo, Sept. 20, 2024. doi: 10.5281/ZENODO.3509134 (cit. on p. 52).
 - [81] E. Bach. "Parasweep: A Template-Based Utility for Generating, Dispatching, and Post-Processing of Parameter Sweeps". In: *SoftwareX* 13 (Jan. 1, 2021), p. 100631. issn: 2352-7110. doi: 10.1016/j.softx.2020.100631 (cit. on p. 52).
 - [82] Y. O. Halchenko et al. "DataLad: Distributed System for Joint Management of Code, Data, and Their Relationship". In: *Journal of Open Source Software* 6.63 (July 1, 2021), p. 3262. issn: 2475-9066. doi: 10.21105/joss.03262 (cit. on p. 52).
 - [83] M. A. Petroff. *Accessible Color Sequences for Data Visualization*. Feb. 29, 2024. doi: 10.48550/arXiv.2107.02270. Pre-published (cit. on p. 52).

Not cited

- [84] A. Beekman, L. Rademaker, and J. van Wezel. "An Introduction to Spontaneous Symmetry Breaking". In: *SciPost Physics Lecture Notes* (Dec. 4, 2019), p. 011. ISSN: 2590-1990. doi: 10.21468/SciPostPhysLectNotes.11.
- [85] U. of Chicago. *Annual Register*. 1893-1930., 1896. 462 pp.
- [86] L. N. Cooper. "Bound Electron Pairs in a Degenerate Fermi Gas". In: *Physical Review* 104.4 (Nov. 15, 1956), pp. 1189–1190. doi: 10.1103/PhysRev.104.1189.
- [87] T. Hazra, N. Verma, and M. Randeria. "Bounds on the Superconducting Transition Temperature: Applications to Twisted Bilayer Graphene and Cold Atoms". In: *Physical Review X* 9.3 (Sept. 17, 2019), p. 031049. doi: 10.1103/PhysRevX.9.031049.
- [88] K.-E. Huhtinen. "Superconductivity and Normal State Properties in Flat Bands". Aalto University, 2023. URL: <https://aaltodoc.aalto.fi/handle/123456789/119970> (visited on 11/27/2024).
- [89] K. Irwin and G. Hilton. "Transition-Edge Sensors". In: *Cryogenic Particle Detection*. Ed. by C. Enss. Berlin, Heidelberg: Springer, 2005, pp. 63–150. ISBN: 978-3-540-31478-3. doi: 10.1007/10933596_3.
- [90] S. Linzen et al. "Quantum Detection Meets Archaeology – Magnetic Prospection with SQUIDs, Highly Sensitive and Fast". In: *New Technologies for Archaeology: Multidisciplinary Investigations in Palpa and Nasca, Peru*. Ed. by M. Reindel and G. A. Wagner. Berlin, Heidelberg: Springer, 2009, pp. 71–85. ISBN: 978-3-540-87438-6. doi: 10.1007/978-3-540-87438-6_5.
- [91] L. Rossi. "Particle Accelerators and Cuprate Superconductors". In: *Physica C: Superconductivity and its Applications* 614 (Nov. 15, 2023), p. 1354360. ISSN: 0921-4534. doi: 10.1016/j.physc.2023.1354360.
- [92] T. Timusk and B. Statt. "The Pseudogap in High-Temperature Superconductors: An Experimental Survey". In: *Reports on Progress in Physics* 62.1 (Jan. 1999), p. 61. ISSN: 0034-4885. doi: 10.1088/0034-4885/62/1/002.

- [93] A. Tollestrup and E. Todesco. "The Development of Superconducting Magnets for Use in Particle Accelerators: From the Tevatron to the LHC". In: *Reviews of Accelerator Science and Technology* 1.01 (2008), pp. 185–210.
- [94] N. Witt. "Electron correlations and unconventional superconductivity in realistic solid state materials and heterostructures". Universität Hamburg.
- [95] C. Yao and Y. Ma. "Superconducting Materials: Challenges and Opportunities for Large-Scale Applications". In: *iScience* 24.6 (June 25, 2021), p. 102541. ISSN: 2589-0042. doi: 10.1016/j.isci.2021.102541.
- [96] C. Zhang et al. "Recent Progress on High-Temperature Superconducting Filters". In: *Superconductivity* 2 (June 1, 2022), p. 100012. ISSN: 2772-8307. doi: 10.1016/j.supcon.2022.100012.

Listings

List of Figures

1.1	Critical surface of a superconductor. For practical applications, this surface is desired to be as large as possible, making it possible to carry high currents and generate strong magnetic fields while not needing to cool the superconductor to very low temperatures. This generally is the case for high-temperature superconductors in comparison to low-temperature superconductors.	2
1.2	BCS-BEC crossover. Reprinted figure with permission from [15]. Copyright 2024 by the American Physical Society.	3
1.3	(a) Twisted Bilayer Graphene (b) Reproduced from [16] with permission from Springer Nature.	4
2.1	Landau free energy and Mexican hat potential (a) Landau free energy f_L for a real-valued order parameter Ψ at different temperatures T . (b) Landau free energy for a complex order parameter Ψ	8
2.2	Ginzburg-Landau solutions for a finite momentum q. (a) Breakdown of the order parameter with q , the critical q_c is the point at which the order parameter is 0. (b) Superconducting current coming from the finite momentum of the Cooper pairs. The maximum of the current with q is called the depairing current j_{dp}	14
2.3	Mapping of the full lattice problem onto a single-site impurity model. This also visualizes the DMFT self-consistency loop: Coming from the full lattice problem, an impurity model is set up, which is then solved to get the self-energy Σ_{imp} , which encompasses all interaction effects. The loop is converged when $\Sigma_{\text{lat}} = \Sigma_{\text{imp}}$, otherwise the impurity self-energy is a new guess for the self-energy of the lattice problem.	22

3.1	Lattice structure of decorated graphene honeycomb lattice. with impurity X hybridized to sublattice site A. Only hopping t between sublattices A and B as well as V between X and A exist. Created using VESTA [70].	31
3.2	(a) Graphene lattice structure with primitive lattice vectors \mathbf{a}_1 , \mathbf{a}_2 and (b) Brillouin zone with reciprocal vectors \mathbf{b}_1 , \mathbf{b}_2 . Both images created with lattpy [75]	32
3.3	Bands of the non-interacting decorated Graphene model	34
4.1	Linear fit for extracting the critical temperature	37
4.2	T (a) Critical temperatures vs V. (b) Gaps vs V	38
4.3	T (a) Critical temperatures vs U. (b) Gaps vs U.	39
4.4	Gaps vs U. for different V	40
4.5	Gap vs q	41
4.6	Gap vs q	42
4.7	Current against q	43
4.8	Temperature fits for xi and lambda	44
4.9	DS	45
4.10	TC against U (also mean field results)	46
4.11	Gap and current vs q.	47
4.12	Temperature fits for xi and lambda	48
4.13	Normalized TC/xi/DS against U (to show BCS-BEC crossover)	49

List of Abbreviations

BCS Bardeen-Cooper-Schrieffer 5, 14, 21

DMFT Dynamical Mean Field Theory 5, 21

BdG Bogoliubov-de Gennes 18

ED Exact Diagonalization 26, 27

DFT Density Functional Theory 30